A Mechanistic Model of the Interaction Between Blue Cones and Blue Cone Bipolar Cells in Macaque Retina

Andreas V. Lønborg

Supervisor: Dr. Stephen J. Eglen

Internship Report
for the Degree
M.Phil. in Computational Biology
from the
Cambridge Computational Biology Institute
Department of Applied Mathematics and Theoretical Physics
University of Cambridge

August 2008

Acknowledgements

Although there are times where producing a thesis certainly seems like a solitary endeavour, this is a delusion. On his own, no man can achieve anything. Hence, I would like to acknowledge the people who have made this thesis possible.

First of all, I would like to express my gratitude towards my academic supervisor, Dr. Stephen J. Eglen, for all the valuable and inspiring discussions during this summer. I am most grateful for his comments and suggestions, which have helped me staying on track during my work with this thesis.

I would also like to thank Prof. Nobuo Kouyama (Tokyo Women's Medical College) and Prof. David W. Marshak (University of Texas) for providing the data, which I have intensively used in this thesis.

All computations in this project have been carried out using `R`. Hence, I acknowledge the `R` project contributors, the authors of the `splancs` package and Dr. Stephen J. Eglen who is the author of the `sjedrp` package.

As studying in Cambridge goes hand in hand with financial obligations, I would like to express my gratitude towards those who have answered my pleas. In particular, I would like to thank EPSRC.

I would like to thank my friend Chris Fisher, my sister Christiane and my girlfriend Susanne for comments and suggestions to my manuscript.

Moreover, as this thesis marks the end of a challenging year in Cambridge studying for the MPhil in Computational Biology, I would like to thank all my colleagues from the course and friends in Cambridge, who have made this year so special. Particularly, I would like to thank Chris Fisher for all the hours we have spent together chatting and drinking coffee.

Finally and most strongly, I would like to thank my greatest love Susanne, who has endured my pursuits in Cambridge with a magnanimity I will never consign to oblivion. Without her endless support and patience in times when I have been most tiresome and too focused on my own work and worries, this thesis would not have existed.

Abstract

Background: The positions of blue cones (BC) and blue cone bipolars (BCBP) have been found to be correlated in the macaque retina [1]. More specifically, BCs, located in the outer nuclear layer (ONL), and BCBPs, located in the inner nuclear layer (INL), both form homotypic mosaics and have an increased chance of being positioned close to each other in the lateral dimension. Furthermore, most BCBPs only form one dendritic contact with BC pedicles, and thus a dendritic string force could cause relative migration.
Methods: In this thesis, a mechanistic model of the BC-BCBP interaction has been developed. It assumes that the BCs are immobile and that the BCBPs can migrate in the INL due to a compromise between the dendritic string force and the intrinsic INL friction force. The model was simulated $N = 99$ times and parameters were selected to optimise the fit with real data fields from Kouyama and Marshak [1]. Density recovery profiles (DRP) and K functions were calculated for both the real data and the simulated data.
Results: Simulated DRPs closely mimic the real data DRPs. In particular, for each of the five retinal fields studied, the simulated DRP for the interaction between BCs and BCBPs has a peak at low distances which is similar to the peak observed in the real data. This peak is the fingerprint for the BC-BCBP correlation.
Conclusion: The mechanistic model devised in this thesis is a candidate model for the unknown mechanism that drives the observed interaction between BCs and BCBPs in macaque monkey. Extensions to other species are likely.

Contents

1 Introduction **1**
- 1.1 The Retina . . . 1
- 1.2 Retinal Research . . . 2
- 1.3 Retinal Mosaics . . . 3
- 1.4 Models for Retinal Mosaics . . . 5
- 1.5 Background for the Project . . . 6
- 1.6 Aims of the Project . . . 8
- 1.7 Outline of the Thesis . . . 8

2 Materials and Methods **9**
- 2.1 Data Sets . . . 9
- 2.2 Modelling Blue Cones and Blue Cone Bipolars . . . 11
  - 2.2.1 Step 1, Generation of Cones . . . 12
  - 2.2.2 Step 2, Differentiation of Blue Cones . . . 13
  - 2.2.3 Step 3, Generation of Blue Cone Bipolars . . . 14
  - 2.2.4 Step 4, Formation of Synaptic Contacts . . . 14
  - 2.2.5 Step 5, Lateral Migration of Blue Cone Bipolars . . . 16
  - 2.2.6 Overview of Fixed Parameters of the Model . . . 20
- 2.3 Quantitative Model Output . . . 22
  - 2.3.1 Regularity Index . . . 22
  - 2.3.2 Density Recovery Profiles . . . 22
  - 2.3.3 K Function . . . 25
- 2.4 Testing Hypotheses . . . 26
- 2.5 Fitting the Parameters . . . 30
- 2.6 Computational Environment . . . 31

3 Results **33**
- 3.1 Optimal Parameters . . . 33
- 3.2 Visual Comparison of Real and Simulated Data Fields . . . 34
- 3.3 Differentiation of Blue Cones . . . 34
- 3.4 Blue Cone Bipolar Dendrites and Migration . . . 38

3.5 Density Recovery Profile Results 48
3.6 Regularity Index and DRP Statistics 49
3.7 Testing Hypotheses 56
3.8 K Functions 58

4 Discussion and Conclusion **63**

A Derivations and Proofs **67**
A.1 Postmigrational Blue Cone Bipolar Position 67
A.2 Proof that $\frac{\partial |l^*|}{\partial l_0} < 0$ 71
A.3 Calculation of Mean Premigrational Dendritic Length 72

References **73**

List of Figures

1.1 Schematic drawing of the eye and the retinal layers 2
1.2 Example of a retinal mosaic 4

2.1 Data field 1 10
2.2 Diagram illustrating the steps of the model 12
2.3 Illustration of BC differentiation 14
2.4 Convergence and divergence of BC-BCBP contacts 15
2.5 Mechanistic diagram of BC-BCBP interaction 17
2.6 Example of density recovery profile 24

3.1 Real data and simulation example, fields 1–3 36
3.2 Real data and simulation example, fields 4–5 37
3.3 Example of simulation of BC differentiation 38
3.4 Example of BCBP dendrites and migration, fields 1–3 39
3.5 Example of BCBP dendrites and migration, fields 4–5 40
3.6 Example of pre- and postmigrational dendritic lengths 42
3.7 Pre- and postmigrational dendritic lengths for each field . . . 43
3.8 Proportion of BCBPs that migrate in each field 45
3.9 Migration distances for each field 46
3.10 Number of synapses for each field 47
3.11 Density recovery profiles, field 1 50
3.12 Density recovery profiles, field 2 51
3.13 Density recovery profiles, field 3 52
3.14 Density recovery profiles, field 4 53
3.15 Density recovery profiles, field 5 54
3.16 L functions 60
3.17 L_{BC} for fields 1 and 3 and a zoom of L_{BCBCBP} for field 1 . . . 61

A.1 Mechanistic diagram of BC-BCBP interaction 68

List of Tables

2.1 Summary statistics for each of the five retinal data fields . . . 11
2.2 Inner nuclear layer depth for each field 19
2.3 Fixed parameters used in the model 21

3.1 Optimised adjustable parameters used in the model 35
3.2 Regularity index and summary statistics based on density recovery profile analysis 55

Chapter 1

Introduction

1.1 The Retina

The vertebrate retina is a laminar structure located in the back of the eye, see Figure 1.1. Its main function is to create a visual perception of the external world. It does so by absorbing incoming photons, and through a cascade of biochemical events in the circuitry of retinal neurons, the visual information carried by the photons (acuity, luminance and colour) is processed and transformed into information packages, which are conveyed via the optic nerve, the optic tract and the optic radiations to the primary visual cortex in the back of the brain.

The perikarya of the retinal neurons are distributed in three nuclear layers [2] (Figure 1.1), with synapses located in two interposed plexiform layers. The outermost layer (in the direction away from the centre of the eye and towards the brain) is the outer nuclear layer (ONL), where the perikarya of photoreceptor rods and cones are located. There are three types of cones: blue cones (BC), green cones and red cones. The names refer to the fact that the peak of the absorption spectra falls in the blue, green and red region of the visual spectrum, respectively. For these reasons, the cones are also called S-cones, M-cones and L-cones, where S, M and L is shorthand for short, medium and long, respectively[1].

It might seem counterintuitive that the layer where the photons are actually absorbed is located furthest away from the incoming light, which implies that before being absorbed in the photoreceptor layer, photons traverse all other retinal layers. However, it has recently been suggested that the Müller cells located in these layers function as optical fibres and guide the incoming

[1]Not all species have three types of cones, but humans and monkeys do. Green and red cones are so similar that they cannot be discerned in labelling experiments.

photons to the photoreceptor layer [3].

The axons of rods and cones protrude into the outer plexiform layer (OPL), where they make synaptic connections with dendrites of bipolar and horizontal cells. The nuclei of bipolar and horizontal cells are both located in the inner nuclear layer (INL). Bipolar cells receive neural signals from photoreceptors and pass them onwards to ganglion cells, see below. Horizontal cells connect to photoreceptors and help regulating the signal which is passed on from the photoreceptors to the bipolar cells.

Amacrine cells are also located in the INL. They receive input from bipolars and other amacrine cells and convey information to bipolars, other amacrine cells and ganglion cells. Their function in the retinal circuitry, however, is not understood.

The inner plexiform layer (IPL) contains the axons of bipolars and dendrites of ganglions and the processes of amacrine cells. Finally, the ganglion cell layer (GCL) contains the ganglion nuclei, which send visual information to the optic nerve.

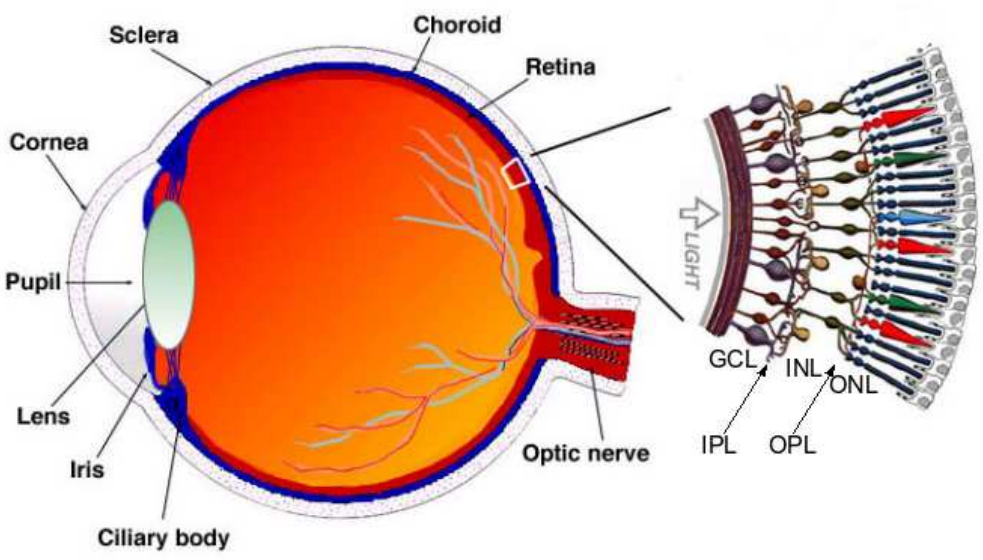

Figure 1.1: A Section of the eye and magnification of the retinal layers. The figure is reproduced from Webvision, http://webvision.med.utah.edu/sretina.html.

1.2 Retinal Research

The retinal neurons produce an immensely complex circuit of connections. Obtaining a full understanding of the retina is an enormous scientific chal-

lenge, and it would include gaining a complete understanding of the individual retinal neurons as well as an understanding of the interplay between neurons.

One line of research has focused on retinal development. Given that there are hundreds of millions of retinal cells, it is clear that all information about the development of the individual cells and their connections cannot be hard-wired in the genome. This implies that research in retinal development focuses on epigenetic mechanisms as well physical principles.

Retinal development can naturally be divided into temporal steps from the 'formation of the eye field' to 'the emergence of light response' [4]. Each step in between has given rise to a vast area of research. See [4] for a recent review, an interesting book where our knowledge of each step of the retinal development is described in a separate chapter.

In order to understand retinal development the job for the scientist is to look for non-random patterns which might give clues about biological mechanisms. A very prominent example of retinal patterns is the way in which the neurons are spatially organised. First of all, as mentioned above, the retina is a laminar structure with each cell type confined within a specified layer. Moreover, a considerable number of individual cell type populations are spatially distributed within a layer in a highly non-random way. Typically, they are distributed regularly in the lateral[2] dimension such that there are no big 'holes' in the pattern. Hence, this type of cell organisation is called *retinal mosaics* because of the way the perikarya and dendrites tile the retina. An example of a retinal mosaic is shown in Figure 1.2. The figure shows the position of BCs from a retinal field from a macaque monkey (field 1 in the data from Kouyama and Marshak [1]).

1.3 Retinal Mosaics

The classic and pioneering quantitative work on retinal mosaics was carried out in the late 1970's, with the discovery by Wässle and Riemann [5] that a selection of retinal cell types (including cone photoreceptors, horizontal cells and ganglion cells) were organised in mosaic patterns. This showed that the neurons must interact in some way. Further, these interactions must be caused by a mechanism at the individual cell level, since a global blueprint of the mosaic would require more information than can be stored in the progenitor cells.

[2]We shall use the word *lateral* to refer to any direction parallel to the retinal layers and the word *radial* for the direction perpendicular to the retinal layers.

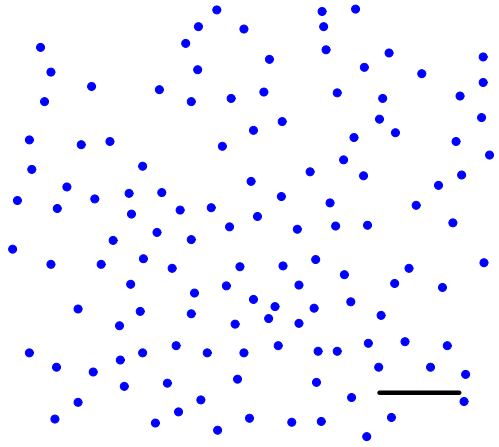

Figure 1.2: BC mosaic from macaque monkey. The size of the circles relative to the size of the field corresponds to approximate real physical BC size (the diameter of BCs is roughly 10 µm). Scale bar is 100 µm.

Wässle and Riemann [5] proposed two generic arguments for the mosaic structure. Firstly, in the case of photoreceptors the obvious advantage of a regular distribution is that 'blind' spots will be avoided. Hence, evolution could have favoured a mechanism, which organises cones into a regular mosaic. Regarding neurons in the INL (called interneurons) and in the GCL, the blind spot argument is less compelling since these neurons do not necessarily have to sample the entire visual field homogeneously. However, they need to make connections to photoreceptors in every part of the retina such that the entire visual field can be sampled. If interneurons were randomly distributed, they would need to have large dendritic areas or to be present in high numbers in order to connect to all photoreceptors. The mosaic pattern would offer a more economic organisation.

The second argument in favour of mosaics [5] was that they might facilitate the formation of connections between layers. This argument is rather *ad hoc* and obviously only applies to two or more layers. So far, no evidence directly supports this hypothesis. As we shall see, this thesis suggests the reverse argument; that regularity in one layer can induce regularity in a neighbouring layer via dendritic connections, i.e. dendritic interactions can create correlated mosaics between layers, not the other way round.

Since Wässle and Riemann reported their pioneering results in 1978, a large number of other empirical studies have identified and quantified mosaics for various cell types and in various species. An abundance of information has been produced. In general, the types of interactions between arrays of cells can be grouped into three categories [1]: (i) between cells of the same type,

(ii) between cells of different types but in the same layer and (iii) between cells (of different type) in different layers. The first type of interaction is also called *homotypic* and the two last types are also called *heterotypic*. Most studies have focused on homotypic mosaics [6–18] (some of these studies have also studied heterotypic interactions, however), but more recently a number of studies have sought to reveal, whether the ubiquity of mosaics of individual cell types could be extended to mosaics of different cells within the same layer [19–24] and to cells in different layers [1, 11, 16, 18, 25, 26].

In general, heterotypic interactions are much less prominent than homotypic interactions. Notable exceptions can be found in [1, 22, 25]. For example, Kouyama and Marshak [1] have found that in macaque monkey, BCs in the ONL and a special subclass of bipolar cells (called blue cone bipolars (BCBP)) in the INL, which connect exclusively to BCs, are spatially positively correlated. This thesis shall deal with this specific interaction.

1.4 Models for Retinal Mosaics

Despite the abundance of empirical observations of retinal mosaics, there is yet no firm understanding of the mechanisms that drive the pattern formation. For recent reviews see [4, Chap. 10] and [27]. In brief, the suggested mechanisms are (i) death of 'misplaced' cells, (ii) lateral inhibition and migration, (iii) dendritic interactions.

In the literature, these mechanisms have been presented in three different ways. Firstly, some studies have hypothesized biological mechanisms, which are claimed to be able to generate mosaics. An example of this is the 'precocious' hypothesis [19], according to which a subset of early maturing cones are regularly distributed across the retina and emit signals which determine the cell fate of neighbouring undifferentiated cells.

The advantage of such biological hypotheses is that the true answer to our questions will necessarily be located in the pool of those hypotheses. The problem, however, is that this pool is indefinitely large and there is little guidance as to which hypotheses might be more likely than others. Also, such hypotheses might be difficult to prove wrong because they tend to be formulated in a way which makes it difficult to make crucial experiments. This probably explains why there are a handful of different candidate hypotheses at the moment.

Another approach is to disregard biological conjecturing and build a purely statistical model and fit it to observed data. Obviously, the disadvantage of this approach is that it is tacit about real biological mechanisms, but the great advantage is that it provides valuable information about the struc-

ture of the mosaic and it can potentially provide us with information about the minimum requirements for a mosaic to form. For example, it has been shown that a simple rule, where every neuron has an exclusion zone around it, is sufficient to generate mosaics which resemble real data [10, 28, 29]. Hence, this simple rule shows that interactions at the local scale can form mosaics. Moreover, this suggests that the researcher looking for biological mechanisms need not look for a global mechanism.

The third and last approach is to use mechanistic models. These combine the advantages of biological hypotheses with the quantitative and falsifiable nature of statistical modelling. A mechanistic model internalises a hypothesized biological mechanism and produces a testable formulation of this mechanism. By comparing the results of the model with real data, the hypothesis will either be rejected or corroborated. The hypothesis is typically based on empirical findings and previous knowledge. Of course, there is no guarantee that a mechanistic model is right, most likely it is wrong, but at least the output of the model will provide information about how likely the model is to be wrong and guide the researcher in a more promising direction. Examples of mechanistic models can be found in [30–32].

For these reasons, I believe that a mechanistic model is scientifically advantageous over biological hypotheses and statistical modelling. This does not imply, however, that these approaches should be banished. It is often a prerequisite for building a mechanistic model to have knowledge about the statistical properties of the biological system.

This thesis presents an original mechanistic model which is used to simulate the interaction between BCs and BCBPs in the retina of the macaque monkey.

1.5 Background for the Project

In 1984, Mariani [33] discovered a new type of bipolar cell which he suspected to connect exclusively to BCs; he therefore named it blue cone bipolar (BCBP). This was confirmed in 1992 by Kouyama and Marshak [7] in a double labelling study where presumptive BCs and BCBPs were labelled simultaneously. In the same year, another bipolar cell type was discovered which also was thought to connect exclusively to BCs [34]. This cell type is OFF-centre[3], whereas the one discovered by Mariani is ON-centre. According to Klug *et al.* [35], however, the alleged OFF BCBP is not exclusively

[3] OFF-centre means that the neuron is depolarised and therefore stimulated when light is projected on the peripheral part of the dendritic field. Conversely, ON-centre means that the neuron is stimulated in response to light projected on the central region.

part of the BC pathway but is a midget bipolar cell, which means that it makes only one connection but this connection can be with different cone types. Hence, the consensus today is that there is only one BCBP type, the one discovered by Mariani in 1984 [33].

My curiosity was triggered by the finding from 1997 by Kouyama and Marshak [1] that the lateral positions of BCs and BCBPs in macaque monkey are positively correlated, i.e. the lateral probability distribution of BCBPs has peaks close to the lateral positions of BCs. In other words, BCBPs tend to be located radially below BCs. I started to speculate about a possible physical mechanism. I noticed that the BCs are packed densely in the ONL and that their axons and pedicles[4] have been shown not to be able to move [36]. Furthermore, and to my great excitement, I noticed that BCBPs tend to contact fewer cones than diffuse bipolars and that a large proportion of them only make one connection [7, 37].

With only one dendritic connection, and assuming that the dendrites exert a string-like force on the BC pedicles and the BCBP, I speculated that the empirically observed positive correlation was primarily caused by migration of those BCBPs with only one dendritic connection to BC pedicles. The mechanism is remarkably simple: if there is a force between two bodies and the two bodies are confined to parallel but separate layers, then this force will tend to reposition the bodies such that they have the same position in the plane of the layers.

In the retina, the neurons cannot migrate freely, so we should not expect to observe a perfect radial alignment of BCs and single dendrite BCBPs. As mentioned, the BCs and their pedicles are probably fixed in the ONL and OPL, respectively. Lateral migration of BCBPs is restricted by a friction force in the INL. The size of this friction force relative to the dendritic string force is a key parameter of the model developed in this thesis.

Finally, in a study by Luo *et al.* [11] it was shown that the positions of both BCs and BCBPs are random in a marmoset monkey, but conditional on the positions of BCs, BCBP positions are nonrandom. This corroborates my working hypothesis that BCBPs are 'followers' in the sense that their position depends on the position of BCs. This thesis is built upon this hypothesis and it is hoped that future work will develop it further.

[4] A pedicle is the part of a photoreceptor cone that connects with the bipolar dendrite. It is located in the OPL.

1.6 Aims of the Project

According to the ideas sketched out in the previous section, the aims of my work have been to

1. develop a mechanistic string and friction force model for the interaction between BCs and BCBPs in macaque monkey retina; it has been a requirement that the model is in accordance with known biological facts about BCs and BCBPs (see previous section);

2. generate the initial patterns of BCs and BCBPs using dimensions and cell numbers identical to the observed ones by Kouyama and Marshak [1]; the simplest possible model for this generation was devised; simplicity is desired in order not to remove focus from the mechanistic model which is the focal point of this project,

3. simulate the mechanistic model based on generated BCs and BCBPs;

4. fit the parameters for the generation of BCs and BCBPs such that the generated patterns resemble real data patterns [1] as well as possible, recognising that given the deliberate choice of a simplistic model, a perfect fit is unlikely and should not be strived for;

5. fit the parameter of the mechanistic model such that the generated correlation between BCs and BCBPs resembles the observed correlation and

6. assess the output of model, primarily the output from the mechanistic part but since this depends on the way the BCs and BCBPs were initially generated, the initial patterns of BCs and BCBPs should also be assessed.

1.7 Outline of the Thesis

In Chapter 2 the details of the model are presented together with the quantitative methods, which have been used to analyse and evaluate it. In Chapter 3 the results are presented, and in the concluding Chapter 4 the results are interpreted and discussed, and suggestions for future research and experiments are given.

Chapter 2

Materials and Methods

2.1 Data Sets

Real data fields were taken from Kouyama and Marshak [1]. The data consist of the spatial positions of BCs and BCBPs in five midperipheral retinal fields (F1–F5) from the same monkey. The data were obtained using a double labelling procedure as described in the paper by Kouyama and Marshak [7].

The retinal data fields were used as templates for the generation of BCs and BCBPs. The dimensions of these five fields and the number of BCs and BCBPs were mimicked in the generation of the artificial fields. These real fields were also used to evaluate the output of the model.

The fields vary in BC density (274–470 mm^{-2}) and BCBP density (544–940 mm^{-2}), with F4 having the highest BC density and F1 having the highest BCBP density. Details of the fields are provided in Table 2.1 on page 11, which is copied from Table 1 in [1]. When it comes to testing the mechanistic model, it is a clear advantage that there is variation between the five fields, since this implies that the model will be scrutinised in five different scenarios.

To get a feel for the real data, Figure 2.1 shows F1. BCs are indicated by filled blue circles and BCBPs are indicated by open circles. The size of the circles relative to the size of the field corresponds to real physical size of BC and BCBP perikarya. BC diameter is approximately 10 µm and BCBP diameter is approximately 8 µm [7]. It is clear that both cell types show regularity since both types tend to tile the field in a mosaic pattern, i.e. there are neither big 'blind spots' nor clusters, which would be expected from a random distribution.

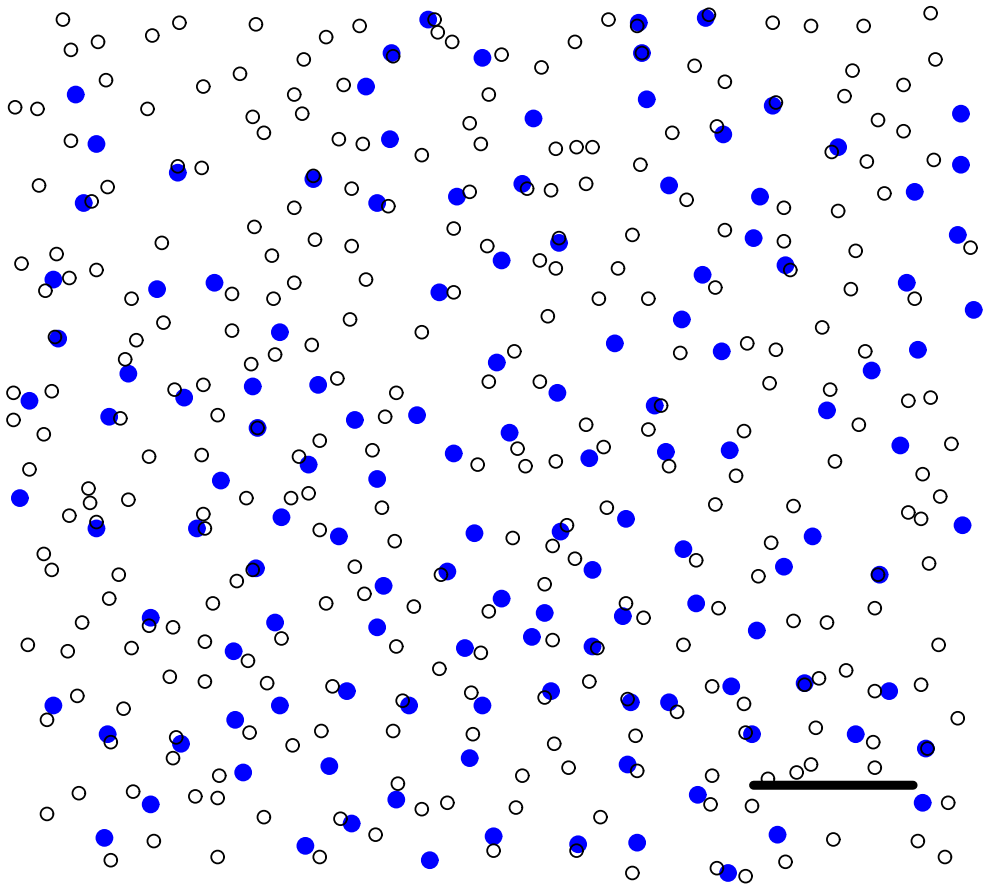

Figure 2.1: The figure shows a real data field, F1, with BCs (filled blue circles) and BCBPs (open circles). The size of the circles relative to the field size corresponds to real physical perikaryon size. Scale bar is 100 µm.

	Monkey 1*				
	Field 1	Field 2	Field 3	Field 4	Field 5
Distance from fovea (mm)	5.8	8.3	5.5	6.8	8.8
Area (mm^2)	0.322	0.314	0.316	0.324	0.333
Number of BCs	130	86	119	152	129
BC density (mm^{-2})	403	274	377	470	388
Number of BCBPs	303	176	268	274	181
BCBP density (mm^{-2})	940	560	849	847	544
Synaptic connections	242	151	213	272	196
Ratio (BCBPs/BCs)	2.33	2.05	2.25	1.80	1.40
BC effective radius (μm)	26.4	38.0	27.2	27.4	32.4
BCBP effective radius (μm)	19.3	21.4	17.9	21.8	28.4

Table 2.1: Overview of the five retinal fields used in this study. The table is reproduced from Table 1 in [1]. *The five fields are all located in the temporal-ventral quadrant in the midperipheral retina. Effective radius is defined in Section 2.3.2.

2.2 Modelling Blue Cones and Blue Cone Bipolars

In this section, the mechanistic model, which I have developed for the interaction between BCs and BCBPs, is described. It should be noted that the generation of the BC mosaic and the initial distribution of BCBPs (before dendritic interactions with BCs induce some BCBPs to migrate) have *not* been made using a mechanistic model. Instead, statistical models have been used. This was deliberately done in order to emphasise that the focus is on the BC-BCBP interaction. Hence, the initial generation of BCs and BCBPs should be as 'neutral' and simple as possible. Obviously, this leaves room for improvement for future research.

The model can naturally be divided into five steps, which correspond to five postulated phases in the development of the BC and BCBP arrays.

1. Generation of undifferentiated cones.
2. Differentiation of BCs.
3. Generation of BCBPs.
4. Formation of synaptic connections between BCBP dendrites and BC pedicles.

5. Lateral migration of BCBPs due to compromise between dendritic string force and INL friction force.

These steps are illustrated in Figure 2.2, where an arrow from A to B indicates that A precedes B in retinal development. Note that the model is neutral about the temporal order of the generation of cones and bipolar cells. The last step, lateral migration caused by the dendritic string force, is the crucial step and marks the original contribution of this thesis.

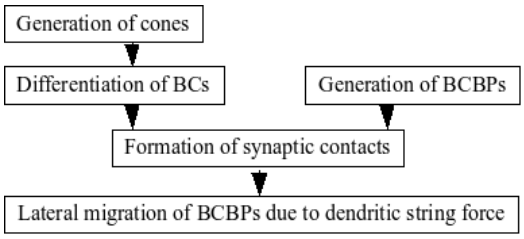

Figure 2.2: The five phases of retinal development which together constitute the model developed here. An arrow from A to B indicates that A precedes B in retinal development.

Before explaining these five steps, I would like to make three important comments. Firstly, all five fields were simulated separately. The description below of the five steps corresponds to the simulation of one generic version of these fields. Secondly, the size of the simulated fields and the number of BCs and BCBPs in each of these mimic the real data. Hence, the dimensions of the simulated fields were set equal to the differences between the maximum and the minimum positions of the real field. This implies that the simulated field densities are identical[5] to the real densities. Densities are obviously key parameters in a study of spatial point patterns. Thirdly, steps 2–5 were repeated $N = 99$ times in order to reduce the uncertainty in the results caused by random sampling and to allow the calculation of Monte Carlo simulation p values.

2.2.1 Step 1, Generation of Cones

The first step in the model is the generation of undifferentiated cones. This was done by drawing from a bivariate uniform distribution on the rectangle with dimensions L_x, L_y, where L_x and L_y are the ranges in the lateral x and y direction, respectively, of perikarya positions in the real data field.

BCs constitute about $a = 10\,\%$ of the total cone population in monkey [17], hence, the number of undifferentiated cones was 10 times the number

[5] There are minor differences, which must be caused be a slightly different definition of field size in [1].

of BCs. Since cones populate the same layer in the retina, they cannot overlap. To circumvent this problem, the cones were iteratively repositioned (by drawing new random numbers) such that they, one after one, satisfied the condition that the distance to the nearest neighbour was at least 12 μm, i.e. an exclusion zone radius of $d_{\text{cone}} = 12\,\mu\text{m}$. The diameter of BCs is around 10 μm [7], so this exclusion zone just avoids physical overlap.

From this point onwards the cones will not move. This simplifying assumption implies that coupled differential equations are avoided in step 5 (see Appendix A.1). The assumption is supported by the fact that the rods and cones in the photoreceptor layer are densely packed [21] and also by a study which shows that the axons and pedicles of BCs do not move [25].

This repositioning of cones is inherently a random process but since the packing of the cones in the fields is rather dense, there is little scope for dramatic variations in the statistical outcome of the process. Hence, these positions were fixed for all Monte Carlo simulations and only BC selection varied, see Step 2.

2.2.2 Step 2, Differentiation of Blue Cones

What separates BCs from green and red cones is the photosensitive protein opsin. Each cone type has it individual variant of this protein. Several studies have showed that the short wavelength opsin (both the protein and the mRNA) specific to the BCs appears earlier in development of mammalian retinae than medium and long wave opsin (macaque [21], human [14], rabbit and rat [38], gerbil and mouse [39]). This conclusion, however, is not reached by all studies. A study by Wikler and Rakic [19] concluded that green and red cones in macaque expressed opsin before BCs, and this has also been hypothesized to be the case in humans [20]. As pointed out in [21], the disagreeing results are likely to be explained by the use of different species and different techniques. In the case of the macaque monkey, it has been explicitly shown [21] that the technique used in [21] is more sensitive than the technique used in [19]. Most studies now conclude that, in general, BC opsin is expressed before green and red cone opsin. In the macaque monkey this conclusion seems to be even more certain.

Based on these observations, BC differentiation has been modelled as follows. A fraction $a = 10\,\%$ of spatially fixed cones differentiate into BCs. Technically, this is done by first sampling n_{BC} BCs from the population of n_{BC}/a cones and then assign an individual exclusion zone d_{BC_i} to each BC. Exclusion zones were assumed to follow a Gaussian distribution with mean μ_{BC} and standard deviation σ_{BC} but with the constraint that they could not be smaller than a hard limit d_{BC}^{min}, i.e. a truncated Gaussian. These

parameters were then estimated by fitting output to data (the criteria used in this process are described in Section 2.3 below). Then for each BC_i, the nearest neighbour distance $d^*_{BC_i}$ is calculated and if $d^*_{BC_i} < d_{BC_i}$, then BC_i was shifted to another and yet undifferentiated cone position leaving behind an undifferentiated cone. This was done iteratively for all BCs until $d^*_{BC_i} > d_{BC_i}$ for $i = 1, \ldots, n_{BC}$.

After step 2, a lattice of cones, some of which BCs, has been sampled. An example of such lattice is shown in Figure 2.3.

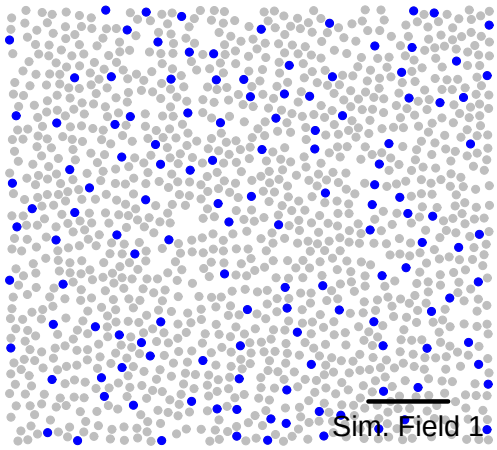

Figure 2.3: Example of simulation of BC differentiation (blue circles) from undifferentiated cones (grey circles), field 1. The sizes of the circles relative to the size of the field correspond to approximate real physical sizes (the diameter of cones is roughly 10 µm). Scale bar is 100 µm.

2.2.3 Step 3, Generation of Blue Cone Bipolars

The n_{BCBP} bipolar cells were generated in much the same way as undifferentiated cones, repositioning them until $d^*_{BCBP_i} > d_{BCBP_i}$ for $i = 1, \ldots, n_{BCBP}$. The only exception was that BCBPs were given individual exclusion zones, drawn from a truncated Gaussian with mean μ_{BCBP}, standard deviation σ_{BCBP} and truncated below at d^{min}_{BCBP}. Again, parameters were estimated by fitting the output to the data, see Section 2.3 below.

2.2.4 Step 4, Formation of Synaptic Contacts Between BCs and BCBPs

When modelling the synaptic contacts between BCs and BCBPs, information about BCBP dendrites should be used. Bipolar cells can be classified

according to the number of dendrites they form. 'Diffuse' bipolars make several connections, whereas 'midget' bipolars make only one connection [2]. One of the key observations about the interaction between BCs and BCBPs is that the BCBP is not a diffuse bipolar in the sense that it contacts fewer cones than diffuse cone bipolar cells. In a study by Kouyama and Marshak [7] it was found that, on average, a BCBP makes 1.2 synaptic contacts with BCs (this number is called the *convergence*), whereas BCs make 1.8 contacts with BCBPs (this number is called the *divergence*). The distribution of contacts is shown in Figure 2.4, which is reproduced from [7]. Almost 70 % of all BCBPs make synaptic connections to only one BC. Less than 30 % make more than one connection.

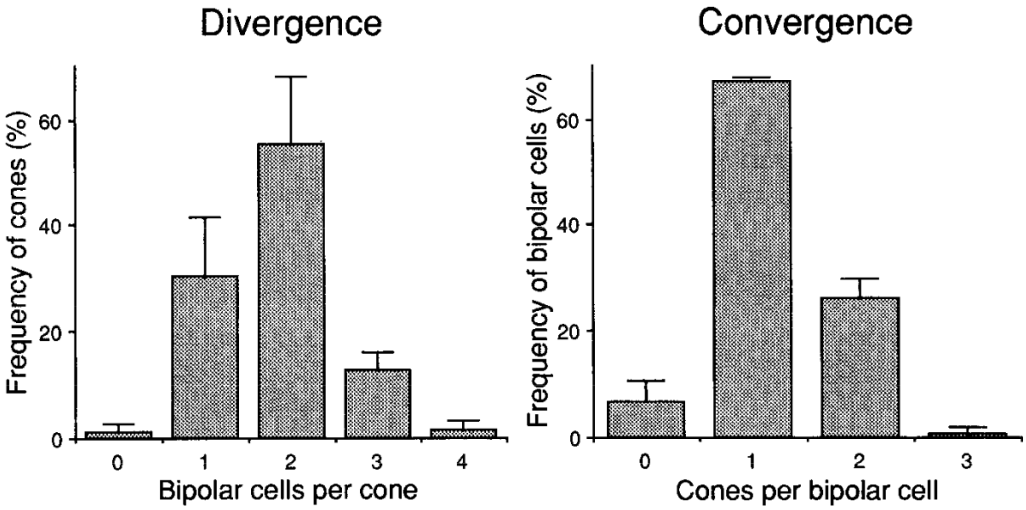

Figure 2.4: Distribution of synaptic connections between BCs and BCBPs. The left panel shows the distribution of the number of BCBP connections which BCs make. This is called the divergence. The right panel shows the distribution of the number of BC connections which BCBPs make. This is called the convergence. Most BCBPs make only one connection, which shows that they, for our purposes, can be considered a 'midget' bipolar. The figure was reproduced from [7].

Optimally, the modelling of synaptic contacts should mimic the distribution shown in Figure 2.4. However, the net dendritic string force exerted on a BCBP with several connections to BCs depends on the position of the BCBP relative to all presynaptic BCs. Hence, it becomes very complicated to determine the equilibrium position analytically. Moreover, modelling several synaptic contacts introduces the problem of how to choose which BCs to contact. It is possible to formulate some probabilistic model, for example a biased random walk model, where dendrites compete for growth in the direction of largest chemical gradient, but such a model is inherently rather

arbitrary since we do not have sufficient knowledge about dendritic growth.

Finally, it can be argued that the inaccuracy introduced by assuming that all BCBPs make only one contact is rather small. To see this, note that if a BCBP makes two connections, then there is a 50 % change of an angle between the two which is smaller than 90° and a 50 % change of an angle which is larger than 90°. When the angle between the two dendrites is smaller than 90°, the two string forces will reinforce each other, and the BCBP will migrate and move significantly closer to *two* BCs. A rough estimate is that this happens for 50 % of the BCBPs. For the other 50 %, the two string forces tend to cancel, and there is no significant migration. Hence, as an *average*, the migration towards BCs by BCBPs with two dendrites can be roughly approximated as the migration towards BCs from BCBPs with only one dendrite. It should be stressed that this argument is only a sketch and does not claim to be rigorous in any way, it is a crude approximation.

Hence, we shall assume that no BCBP can make more than one contact. Furthermore, following the observation in [7] that no dendrite was longer than 50 μm, we shall assume that BCBPs, with a lateral distance of more than $l_{\max} = 44\,\mu\text{m}$ from the nearest BC, do not form contacts[6].

Under these assumptions, each BCBP was connected to the nearest BC. Finally, and also following an observation in [7], BCs are restricted to have a maximum of four connections with BCBPs (see also Figure 2.4). If it turns out that a BC has more than four connections, connections are removed by random until it only has four connections.

2.2.5 Step 5, Lateral Migration of Blue Cone Bipolars Due to Compromise Between Dendritic String Force and INL Friction Force

At this stage, BCBPs have formed connections to BCs and now face two forces: (i) the dendritic string force and (ii) a friction force which resists migration in the INL. BCBPs are assumed to migrate as a reaction to these two forces. The question remains, how to model these forces. In the following, I will state the assumptions for the physical modelling of the system and present a formula for the equilibrium position of BCBPs as a function of the initial position, the ratio between the friction and string force and the vertical distance between the BCBP and the BC pedicle. The physical situation is sketched in Figure 2.5.

[6] A vertical separation of 23.2 μm has been assumed. In order to understand where this number comes from, the reader is referred to the description of Step 5 below.

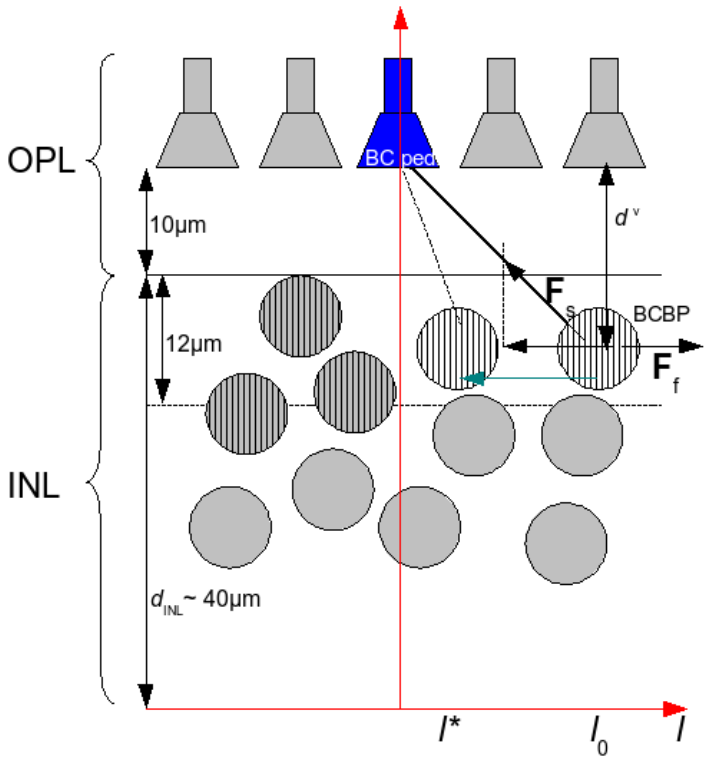

Figure 2.5: Diagram of the mechanistic model. BC pedicles are fixed in the OPL, whereas BCBPs which are less than $3 \cdot r_{BCBP} = 12\,\mu m$ from the INL-OPL interface can migrate laterally within the INL. BCBPs are distributed in the INL with mean distance from the INL-OPL interface of a third of the INL depth and with a standard deviation of 0.11 of the INL depth. This implies that 38 % of BCBPs have the potential to migrate. The relative number of BCs and BCBPs, the radial distribution of BCBPs and the size of BCBPs match the real retina. BCBPs which are located deeper in the INL are assumed to be immobile because their dendrites will potentially not contact a BC pedicle in a straight line because of other BCBPs blocking the way. BCBPs which can potentially migrate have been hatched in the diagram, and BCBPs which cannot migrate are unhatched. An example of a BCBP migration is shown. The hatched BCBP with white background is connected with the blue BC pedicle. The BCBP is under influence of string force $\mathbf{F}_s$ and friction force $\mathbf{F}_f$. These forces are indicated with black arrows. The projection $\tilde{\mathbf{F}}_s$ of $\mathbf{F}_s$ on the lateral plane is also indicated with an arrow. The BCBP migrates from initial position l_0 to postmigrational position l^*. The turquoise arrow indicates the migration. The dashed line indicates the postmigrational dendrite. Red arrows indicate the coordinate axes. Relevant depth variables and magnitudes are indicated.

We shall assume that the dendritic string force exerted on $BCBP_i$ is given by the three-dimensional vector $\mathbf{F}_i^s$ with length F_i^s.

Not all BCBPs are influenced by a string force, however. BCBPs are located in the INL, but the INL is wider than the diameter of a single BCBP. Hence, BCBPs are not located in the same plane. We assume that if another BCBP can be positioned 'above' a BCBP then this BCBP cannot move. Immobile BCBP are indicated as non-hatched circles in Figure 2.5. Therefore, it is assumed that the possibility of migration is restricted to BCBPs with centres less than three times the BCBP radius r_{BCBP} from the INL-OPL interface. The radius of a BCBP perikaryon is estimated to be $r_{BCBP} = 4\mu\text{m}$ [7]. By restricting the number of BCBPs which can migrate, the correlation between BCs and BCBPs which will be seen in the output is effectively reduced.

The vertical distance d_i^v between the constant level of BC pedicles and $BCBP_i$ is drawn from a Gaussian distribution with mean $\mu^v = 10\mu\text{m} + \frac{1}{3}d_{INL}$ and standard deviation $\sigma^v = 0.11\, d_{INL}$, where d_{INL_i} is the depth of the INL at the part of the retina where BCBP i is taken from. Table 2.2 shows crude estimates of the INL depth at the locations of each of the fields. These numbers are based on Figure 2 in [7].

We can explain the expressions for μ^v and σ^v by a number of observations made by Kouyama and Marshak [7]: (i) BCBPs are, on average, located a third of the INL depth from the INL-OPL interface (Figure 7 in [7]), and (ii) with a standard deviation of $\sigma^v = 0.11\, d_{INL}$, and (iii) the distance from the BC pedicles to the INL-OPL interface is approximately 10 µm (Figure 2 in [7]).

This also explains how the vertical distance between BCBPs and BCs was calculated in Section 2.2.4 describing step 4. Assuming a INL depth of 40 µm gives a mean vertical distance between BCs and BCBPs of $\mu^v = 23.2\,\mu\text{m}$. Assuming an INL depth of 40 µm in all five fields is not optimal (see Table 2.2), but it makes little difference to the maximal length of projections of dendrites onto the plane.

Given the mentioned parameter values, we can calculate that 38 % of BCBPs have the potential to migrate[7].

We shall also assume that the friction force $\mathbf{F}_i^f$ on $BCBP_i$ is velocity independent and directed against the direction of migration. If we regard the BCBP as a particle moving through a viscous fluid then it would seem natural to assume a velocity dependent friction force since this is the standard result from fluid dynamics (*linear drag*). The problem, however is that this will make the equilibrium BCBP position independent of initial position (see

[7] $P(X < 12) = 0.38$, where $X \sim N\left(\frac{40}{3}, 0.11 \cdot 40\right)$.

	Monkey 1				
	Field 1	Field 2	Field 3	Field 4	Field 5
INL depth, d_{INL} (μm)	40	20	40	30	15

Table 2.2: Depths of the INL for each field. These values are crude estimates based on Figure 2 in [7].

Appendix A.1), which also seems unlikely.

We can now explain how the BCBPs migrate. If the length of the projection of the string force onto the horizontal plane is smaller than the friction force, then nothing happens. If it is greater than the friction force, then the BCBP accelerates and linear migration in the direction of the BC projection commences with the friction force constantly opposing movement[8]. As the BCBP moves closer to the BC projection the dendrite will loose its tautness, but it is assumed that the dendrite becomes shorter, such that it is always taut and carries a force. Also, as the BCBP moves closer to the BC projection, the projected string force onto the BCBP plane decreases. At some point, the BCBP will have moved so close to the BC that the projection of the string force is equal to the friction force. From this point, the BCBP will start to decelerate, eventually coming to rest at its new equilibrium position.

The new equilibrium position can be derived by writing down the equation of motion for the system and finding the steady state (where acceleration and velocity are zero). The derivations and the final result are given in Appendix A.1. The result is restated here in equation 2.1.

If $l_{0,i}$ denotes the initial lateral distance between BCBP i and the BC pedicle it connects to, if d_i^v denotes the vertical distance, and if $F_{(f/s),i}$ denotes the relative friction-to-string force, then we can write the postmigrational position l_i^* of BCBP i relative to the BC pedicle projection as

$$l_i^* = \frac{2F_{(f/s),i}\sqrt{l_{0,i}^2 + (d_i^v)^2} - \left(\left(F_{(f/s),i}\right)^2 + 1\right) l_{0,i}}{1 - \left(F_{(f/s),i}\right)^2}. \tag{2.1}$$

The new position of $BCBP_i$ will be on the straight line connecting (i) the projection of the BC pedicle onto the plane of $BCBP_i$ and (ii) the initial $BCBP_i$ position, and at a distance of $|l_i^*|$ from the BC pedicle projection. Note that l_i^* can be negative, indicating that the BCBP has passed the BC pedicle projection.

[8] We do not discern between static and dynamic friction forces.

It should be noted that the postmigrational position only depends on the ratio between the friction and the string force $F_{(f/s)}$. Effectively, there is therefore only one force parameter in the model. This is both good and bad. Given that we have no *a priori* information about the values of these forces, it is an advantage that we only have to deal with one arbitrary parameter. It also makes the model more parsimonious, and more parsimonious models are inherently preferable, *ceteris paribus*. On the other hand, however, fitting the model does not enable us to estimate both forces, only the relative force can be estimated. But since we are not interested in these values *per se*, we consider it to be a nice feature of the model that it only depends on the relative force.

In the simulations, each BCBP was assigned a relative force, drawn from a Gaussian distribution with mean $\mu_{f/s}$ and standard deviation $\sigma_{f/s}$.

There is one problem with the migration model that has been sketched. Since it considers each BCBP separately, it does not take into account that BCBPs might collide during migration. Also, the migration might have moved some BCBPs so close to each other (in the lateral plane) that the exclusion zone is no longer satisfied. To circumvent these problems, those BCBPs, which in the end state have a neighbour which is too close, are considered. From this set of BCBPs, the BCBPs which have migrated are selected and their migration are reversed in small steps of equal size[9]. After each step, the exclusion zones are evaluated. This continues until all exclusion zones are satisfied again. This process effectively implies that collisions are modelled as events that bring BCBPs to a stop. Biologically, this is probably not terribly wrong.

Alternatively, a full dynamical simulation could have been pursued, but it is unlikely that anything would have been gained from this. After all, the model is a sketch and does not involve time and does not claim to be so physically accurate that dynamical simulations are warranted.

2.2.6 Overview of Fixed Parameters of the Model

As an overview, Table 2.3 on Page 21 summarises the values of all parameters, which have been used in the modelling and have not been manipulated to improve the fit. Hence, these parameters are called *fixed parameters*.

[9] In the case of a pair of BCBPs which are too close and which have both migrated, making the reverse steps of equal size implicitly assumes that they migrated simultaneously. In real retinas, all BCBPs will not commence migration at the same time, but we shall ignore this; after all the model does not claim to be perfectly accurate.

	Monkey 1				
	Field 1	Field 2	Field 3	Field 4	Field 5
Number of BCs, n_{BC}	130	86	119	152	129
Number of BCBPs, n_{BCBP}	303	176	268	274	181
Ratio (BCBPs/BCs)	2.33	2.05	2.25	1.80	1.40
Field dim. x, L_x (µm)	602	594	595	603	602
Field dim. y, L_y (µm)	541	534	535	542	558
Area, $\|A\|$ (mm^2)	0.326	0.317	0.318	0.327	0.336
BC density, D_{BC} (mm^{-2})	399	271	374	465	384
BCBP density, D_{BCBP} (mm^{-2})	930	555	842	838	539
Cone excl. zone, d_{cone} (µm)	12	12	12	12	12
Fraction of BCs among cones, a	0.1	0.1	0.1	0.1	0.1
BCBP radius, r_{BCBP} (µm)	4	4	4	4	4
INL depth, d_{INL} (µm)	40	20	40	30	15
BC pedicle to INL-OPL (µm)	10	10	10	10	10
Dist. from BCBP to BC ped. (mean), μ^v (µm)	23.2	16.6	23.2	19.9	14.95
Dist. from BCBP to BC ped. (SD), σ^v (µm)	4.4	2.2	4.4	3.3	1.65
Max. dendr. length, $l_{\max}$ (µm)	44	44	44	44	44
SD of relative force, $\sigma_{(f/s)}$	0.1	0.1	0.1	0.1	0.1

Table 2.3: Fixed parameters. Parameters which have not been adjusted during the fitting of the model.

2.3 Quantitative Model Output

The model described above is of little value if it cannot be assessed quantitatively and compared with real data. The statistics of spatial point patterns (as retinal neurons essentially are) are rather involved, but there are some relatively simple ways to evaluate whether the generated BC and BCBP layers have the same characteristics as the real data. The problem is to decide on what characteristics to look for.

Considering that the model, as sketched out above, takes the number of cells and the dimensions of the field for given, this implies that the model cannot influence the densities. All the model can influence is the relative lateral distances between cells. In the spatial point pattern literature, properties of random variables related to the relative positioning of points are called *second-order properties* [40]. Hence, second-order statistics should be used to evaluate the model.

Four different, but related, second-order statistics are used here, (i) regularity index, (ii) density recovery profile (DRP) analysis [41] (with related statistics), (iii) K function analysis [40] and (iv) G function analysis [40].

Each simulation of the model will produce some statistics (for each field), and because the model is simulated $N = 99$ times we can use the Monte Carlo framework to formulate and test hypotheses about the output of the model. In the following, the statistics are described.

2.3.1 Regularity Index

The regularity index RI is the most common second-order summary statistic of a spatial point mosaic. It is defined as the mean of the nearest neighbour distances divided by the standard deviation of the nearest neighbour distances [5]. Intuitively, the larger the mean distance (for a given standard deviation), the more regular is the pattern, and the smaller the standard deviation (given the mean) the more regular is the pattern. Hence, RI increases with increasing regularity. For *complete spatial randomness* (CSR) it can be shown that $RI = \sqrt{\pi/(4-\pi)} \approx 1.913$ [42]. Hence, if $RI > 2$ the pattern has some degree of regularity.

2.3.2 Density Recovery Profiles

Another and more sophisticated way of evaluating the regularity of a spatial point pattern is to use *density recovery profiles* (DRP) [41]. The idea is to determine the density of a population of points as a function of distance from a reference point. If this is done for all reference points in some population,

the densities can be averaged to provide the DRP. Typically the density is estimated in 5 or 10 μm bins, here 10 μm bins are used up to a maximum distance of 100 μm, i.e. there are $J = 10$ bins. The advantage of DRP, compared to making a nearest neighbour histogram, is that DRP uses all points instead of only the nearest neighbours. It therefore carries more information about the data than a nearest neighbour statistic. It is called DRP because of the fact that for regular patterns, the density will converge to the average density as the distance increases.

As indirectly indicated, DRPs can be calculated for one population of points (auto DRP or aDRP) or for two populations. In the latter case, the reference cells are taken from one population and the density of the other population around the reference cells is then estimated (cross DRP or cDRP). An example of DRPs (for field 1) is shown in Figure 2.6.

The dip in the BC and BCBP aDRP reflects the homotypic exclusion zones. The cDRP has a significant peak at small distances, indicating that BCs and BCBPs are positively correlated at short distances.

Points which are close to the edge of the sampled region introduces a bias in the estimation of the DRP since a part of their surroundings is void of points. If it is assumed that the unsampled region is similar to the sampled region then this can be used to compensate, such that points close to the edges do not have to be excluded. This compensation scheme is built into the `R` package `sjedrp`.

In the case of CSR, the DRP function will obviously be flat. Hence, this suggests that the DRP can be tested against the hypothesis of CSR, see Section 2.4 below.

Based on the DRP analysis, a number of summary statistics can be calculated. These are defined below.

Effective radius The *effective radius* r_{eff} is a measure of the exclusion zone around points in the reference population. The idea is that when the pattern is regular, the exclusion zone around each reference point will imply that there will be a dip in the DRP for small values of the interpoint distance. One way to summarise the size of this dip is to ask how many points would have to be added to this region in order to eliminate the dip such that the DRP becomes flat with a level equal to the overall density. This number of points is then converted into an area using the overall density. The effective radius is simply the radius of a circle with this area. The `sjedrp` package automatically calculates r_{eff}.

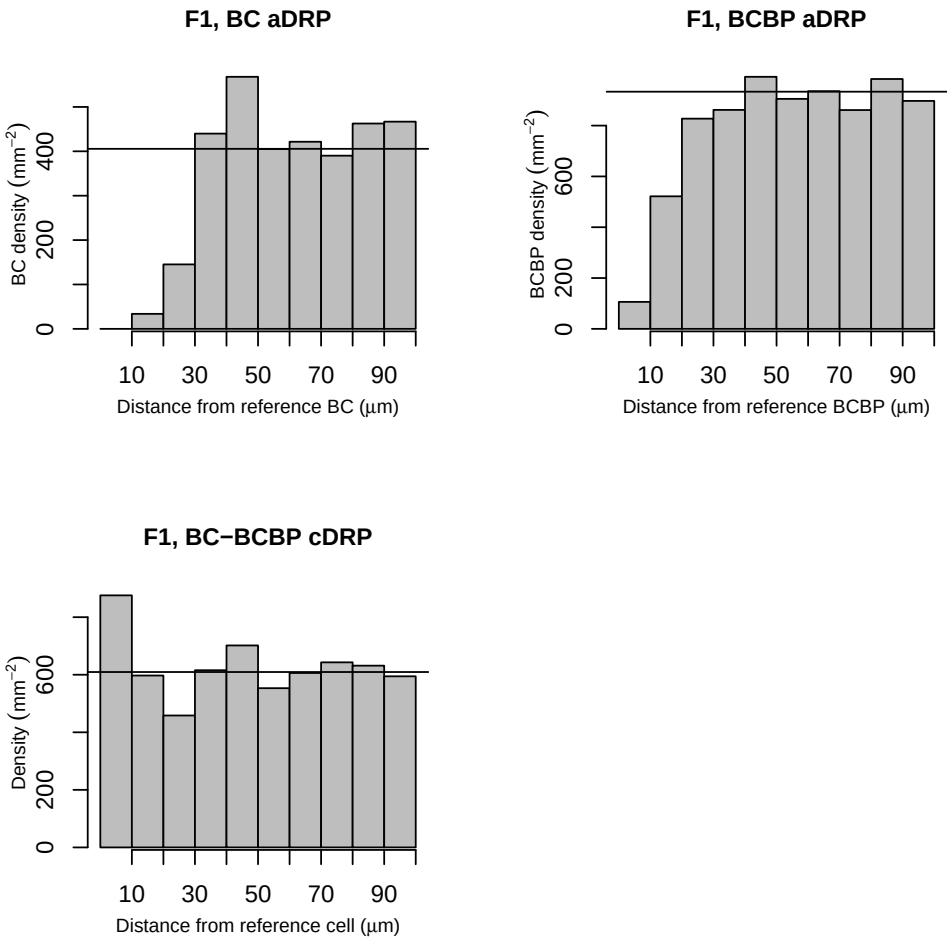

Figure 2.6: DRP for field 1 real data. The dip in the BC and BCBP DRP reflects the homotypic exclusion zones. The cDRP has a significant peak at small distances, indicating that BCs and BCBPs are positively correlated at short distances.

Maximum radius The *maximum radius* $r_{\max}$ is merely the maximum exclusion zone which still makes it possible to fit the given number of cells into the given area. Since a hexagonal array is the optimal method of packing circles, the maximum radius is simply $r_{\max} = \frac{\sqrt{4/3}}{D}$, where D is the overall density [41].

Packing factor The main reason for defining the maximum radius is that it provides an upper limit for the effective radius [41]. The *packing factor* p is defined as $p = (r_{\text{eff}}/r_{\max})^2$, it ranges between 0 (CSR) and 1 (hexagonal structure).

2.3.3 K Function

Instead of the DRP, which is a density measure, a cumulative variant could be considered. One such variant is the K function [40], which basically counts the number of pairs of points which are within a certain distance t. In the univariate case, it is defined as [40]

$$K(t) = \lambda^{-1} E[\ \#\ \text{points within distance } t \text{ of arbitrary reference point}], \tag{2.2}$$

where λ is the (constant) intensity, i.e. the average density $n/|A|$, where n is the number of points and |A| is the area of the field A.

In the bivariate case with subpopulations i and j, the K function (with population i as reference population) is defined similarly

$$K_{ij}(t) = \lambda_j^{-1} E[\ \#\ \text{type } j \text{ points within distance } t \text{ of arbitrary type } i \text{ point}]. \tag{2.3}$$

If a univariate spatial point process is random (CSR) then $K(t) = \pi t^2$, and if two variables are independent in a bivariate spatial point process then $K_{12}(t) = \pi t^2$ [40]. This implies that testing against CSR and independence is possible.

For plotting purposes, we can define the function $L(t) \equiv (K(t)/\pi)^{1/2}$. Under assumption of CSR and/or independence, $L(t) = t$, which makes visual inspection of L plots an easy way to assess these hypotheses.

In order to estimate the K function, note that $\lambda K(t)$ is the number of points within distance t of an arbitrary point. Since there are n arbitrary points and since we can write this as $n = \lambda|A|$, it follows that there will be $\lambda^2|A|K(t)$ ordered pairs of points (each pair is counted twice) which are within a distance t. This number is most easily estimated as the number of observed ordered pairs, which we can write as $\sum_{i=1}^{n} \sum_{j \neq i} I\left(||\mathbf{x}_i - \mathbf{x}_j|| < t\right)$,

where $I(\cdot)$ is the indicator function which is 1 if the argument is true and 0 otherwise and $\mathbf{x}_i$ is the position of point i.

The definition of K assumes that the points are not restricted to a finite plane. In practice, however, A is bounded and the probability of observations outside the area is zero. If we are willing to assume stationarity and isotropy, then we can easily compensate for this. Under these assumptions, the proportion of the circumference of the circle centred at $\mathbf{x}$ and with radius u which is inside the area A will be identical to the conditional probability of observing an event inside A given that we know that an event takes place at a distance of u from $\mathbf{x}$.

Let us by w_{ij} denote the proportion of the circumference of a circle centred in $\mathbf{x}_i$ with radius $||\mathbf{x}_i - \mathbf{x}_j||$, which is inside the area A. To compensate, we can therefore simply divide the binary counts $I\left(||\mathbf{x}_i - \mathbf{x}_j|| < t\right)$ by these weights w_{ij}. Hence, in the univariate case

$$\hat{K}(t) = \frac{A}{n^2} \sum_{i=1}^{n} \sum_{j \neq i} w_{ij}^{-1} I\left(||\mathbf{x}_i - \mathbf{x}_j|| < t\right), \tag{2.4}$$

and in the bivariate case

$$\hat{K}_{12}(t) = \frac{A}{n_1 n_2} \sum_{i=1}^{n_1} \sum_{j=1}^{n_2} w_{ij}^{-1} I\left(||\mathbf{x}_{1,i} - \mathbf{x}_{2,j}|| < t\right), \tag{2.5}$$

where n_1 is the number of events in population 1, n_2 is the number of events in population 2 and subscripts 1 and 2 on $\mathbf{x}$ refer to population 1 and 2, respectively.

G function In addition to the univariate K function, a cumulative nearest neighbour function $G(t)$ can be calculated as

$$G(t) = \frac{1}{n} I(y_i \leq t), \tag{2.6}$$

where y_i is the nearest neighbour distance of point i. $G(t)$ is simply the fraction of points in a population with a nearest neighbour distance less than t.

2.4 Testing Hypotheses

There are three kinds of hypotheses that would be relevant to test:

1. Is the output of the model different from what could be produced at random, i.e. does the model introduce any structure to the data?

2. Is the output of the model different from the observed data, i.e. is the model doing the right thing?

3. Are the fields significantly different from each other?

The first hypothesis should be rejected before attempting to test the second (assuming that data is nonrandom). Note that acceptance of the second hypothesis does not imply that the model is *right*, it merely suggests that the model *could* be right and should be taken serious as a candidate model in future experimental and theoretical work.

In order to be able to test hypotheses and draw inference, we need to formulate a statistical model that can capture the variation in the data.

Within the DRP framework the most straight forward is to regard the density of a given bin as a result of the combination of what field and what bin the given bin represents. If we denote the DRP density of field i, bin j and replication k by y_{ijk}, then the model M reads.

$$y_{ijk} = \alpha_{ij} + \epsilon_{ijk}, \quad \epsilon_{ijk} \sim N(0, \sigma^2), \tag{2.7}$$

where $i = 1, \ldots, 5$, $j = 1, \ldots, 10$ and $k = 1, \ldots, 99$. In other words, for each combination of field i and bin j, the densities y are 'drawn' from a Gaussian distribution with a specific mean α_{ij}. The variances of these 50 Gaussians are assumed to be identical, σ^2.

Given this full model with 51 parameters (α_{ij} and σ), hypotheses about restricted models can be tested. One way to do this is to estimate the restricted model and compare the residuals of the full and restricted model, taking into account that the restricted models has less parameters. This is the essence of likelihood ratio tests.

We can also test hypotheses outside the DRP framework. We can test whether there is a difference between a statistic calculated based on real data and calculated based on simulated data. For example, we can test whether the mean (across simulations) of the regularity index RI for field i is significantly different from the real data value. This is most easily done using a standard t-test. If x denotes a simulated vector of length N and μ_0 is the real data counterpart, then the test statistic is simply

$$T = \frac{\bar{x} - \mu_0}{sd(x)/\sqrt{N}} \sim t(N-1) \tag{2.8}$$

Finally we can test hypotheses about the K function. Because of the non-standard theory of spatial point patterns, test statistics are less standard, see below.

We now explain the various tests in more detail.

Test of hypothesis 1 in DRP framework In the univariate case this is a test of CSR and in the bivariate case this is a test of independence.

One way to make this test is to ask whether a DRP (auto or cross) of a given field i is flat, i.e. all bins $j = 1, \ldots, J$ have the same height. In terms of the statistical model M from above, the hypothesis pair reads

$$H_0 : \alpha_{i1} = \alpha_{i2} = \ldots = \alpha_{iJ} \quad H_1 : \text{non } H_0. \tag{2.9}$$

To test this, simply estimate the model under H_0 (restricted model) and under H_1 (full model) and make an ANOVA. This is a standard procedure in R.

Another way of testing the independence between BCs and BCBPs it to compare the cDRPs before and after migration. Prior to migration, the cDRP should be flat. This can be implemented in the general model M by simply adding a subscript indicating whether an observation is from before or after migration. Alternatively, individual bins before and after migration can be compared using a simple t-test to compare the means of two samples (remember that there are $N = 99$ observations in each of these samples). Assuming that the two distributions have the same variances (as we also assumed in M) and that they are drawn from asymptotically normal distributions, the test statistic is

$$T_j = \frac{\bar{y}_{2,j} - \bar{y}_{1,j}}{\sqrt{\frac{s_{1,j}^2 + s_{2,j}^2}{N}}} \sim t(2N - 2), \tag{2.10}$$

where $\bar{y}_{1,j}$, $\bar{y}_{2,j}$, $s_{1,j}$ and $s_{2,j}$ are the mean values and standard deviations of the densities in bin j before and after the lateral migration of BCBPs, respectively. This test is then performed for each bin j. Of course it is easier to accept that one pair of bins is identical than that entire DRPs are identical.

Finally, a variant of the type 1 hypothesis is to ask, whether migration has had an impact on BCBPs. Again, this can be tested by simply comparing bins from the BCBP aDRP before and after migration.

Test of hypothesis 2 in DRP framework Testing against data can either be performed within the statistical model M or with the use of t-tests. Using the statistical model, we can ask whether an entire field is significantly different from data. In this case, the hypothesis pair reads

$$H_0 : \alpha_{i1} = a_{i1}, \ldots, \alpha_{iJ} = a_{iJ} \quad H_1 : \text{non } H_0, \tag{2.11}$$

where a_{ij} are the real data density of field i bin j. Using t-tests we can only compare pairs of bins.

Test of hypothesis 2 in K function framework Within the K function framework we only wish to test for difference between model output (K_{BC}, K_{BCBP} and $K_{BC,BCBP}$) and data. The idea is simple. The closer the average simulated K function is to the real data K function, the more confidence we have in the model. One way to summarise each of the $N+1$ K functions (N simulated and 1 real) is to calculate the following test statistic

$$T^i = \int_0^{t_{\max}} \left[\sqrt{K^i(t)} - \sqrt{\bar{K}^i(t)} \right]^2, \quad i = 1, \ldots, N+1, \tag{2.12}$$

where $K^1(t)$ is the real data K function and $K^i, i = 2 \ldots, N+1$ is the K function from the $(i-1)$'th simulation, $\bar{K}^i(t) = \frac{1}{N} \sum_{j \neq i} K^j(t)$ and $t_{\max}$ is chosen based on the alternative hypothesis [40]. Typically $t_{\max}$ is set to a quarter of the field dimension, which would be around 150 µm in this case. Here, however $t_{\max} = 100\,\mu\text{m}$, since we do not care about what happens beyond 100 µm[10]. In order to test hypotheses about K_{12}, simply substitute K_{12} for K in these expressions.

A high value of T^i indicates that $K^i(t)$ is very different from the other K^j, $j \neq i$. If the T^i are ranked in decreasing order then rank$(T^1)/100$ will provide the fraction of T^i values which are higher than T^1 and this can be used as a Monte Carlo p value of a test that T^1 is from the same distribution as T^i, $i = 2, \ldots, 100$. If this hypothesis is accepted at the chosen significance level, then the model fits the data sufficiently well.

Test of hypothesis 2 based on statistics calculated from DRP Standard t-tests can be used to test if simulated statistics are significantly different from real data statistics. The following statistics have been tested: RI, r_{eff}, $r_{\max}$, D and p.

Test of hypothesis 3 in DRP framework Finally, the model M can be used to test whether fields i_1 and i_2 are significantly different.

$$H_0 : \alpha_{i_1 1} = \kappa\alpha_{i_2 1}, \alpha_{i_1 2} = \kappa\alpha_{i_2 2}, \ldots, \alpha_{i_1 J} = \kappa\alpha_{i_2 J} \quad H_1 : \text{non } H_0, \tag{2.13}$$

where κ is included in order to avoid effects from different macroscopic field densities. Alternatively, bin densities can be normalised by the macroscopic density before estimating the model M.

[10] We could have chosen $t_{\max}$ even smaller, but since the upper limit in the DRP analysis is 100 µm, $t_{\max} = 100\,\mu\text{m}$ was a good choice.

2.5 Fitting the Parameters

In order to obtain the best possible fit with data, exclusion zone parameters for both BCs and BCBPs as well as the ratio of mean friction force and mean string force were manually adjusted. More specifically, exclusion zones were drawn from truncated Gaussians (a random number is drawn from a Gaussian and if it falls outside the acceptable range, it is drawn again). The following list includes all parameters that were adjusted manually.

1. BC exclusion zone
   (a) Mean from nontruncated Gaussian, μ_{BC}
   (b) Standard deviation from nontruncated Gaussian, σ_{BC}
   (c) Minimal exclusion zone, d_{BC}^{min}
2. BCBP exclusion zone
   (a) Mean from nontruncated Gaussian, μ_{BCBP}
   (b) Standard deviation from nontruncated Gaussian, σ_{BCBP}
   (c) Minimal exclusion zone, d_{BCBP}^{min}
3. Mean of ratio between friction force and string force, $\mu_{f/s}$

The parameters relating to BC exclusion zones (μ_{BC}, σ_{BC} and d_{BC}^{min}) were chosen to maximise the p value from the test of the K_{BC} function. Even though generation of a reliable BC mosaics was not the main task of this study, it was important for the reliability of the outcome of the migration model that the simulated BC data were fairly similar to the real data[11].

The parameters relating to BCBP exclusion zones (μ_{BCBP}, σ_{BCBP} and d_{BCBP}^{min}) and the mean force ratio $\mu_{f/s}$ were chosen to maximise the p value from the test of the K_{BCBP} and $K_{BC,BCBP}$ function and to produce cDRP plots which were as similar to the real data cDRP plots as possible. There is no objective way to balance these three objectives against each other, hence this maximisation procedure was rather *ad hoc*. More sophisticated methods could be probably be devised, but it has not been considered worthwhile to attempt this. As we shall see in the next chapter, the results are convincing even with this somewhat *ad hoc* optimisation scheme.

It has been a deliberate aim to keep the number of adjustable parameters as low as possible. The more parsimonious the retinal model, the more

[11] In the first few weeks of the project, real BC data were used instead of simulated data in order keep the focus on BCBP migration, but this was subsequently changed such that the final model is completely simulated.

powerful the results (if they fit data reasonably) and the more the intrinsic structure of the model should be trusted. The mechanistic part (step 5) is the cornerstone of the model and is the original contribution of this thesis. It is therefore worthwhile to notice that the *only* adjustable parameter directly relating to the mechanistic part of the model is the relative friction force $\mu_{f/s}$.

2.6 Computational Environment

All computations were performed in `R` version 2.6.1 using the standard packages `stats`, `class` and `graphics` and the specialised packages `splancs` and `sjedrp`. `splancs` was used to compute K and G functions, `sjedrp` was used to compute DRPs. `R` code can be provided upon request.

Chapter 3

Results

In this chapter, the results of running the model and simulating the five retinal fields are presented and compared with the real data fields. As mentioned in the previous chapter, the modelling of the BCBP migration is the original contribution of this thesis. Hence, assessment of the model should focus on the last step (step 5). In other words, assessing the statistical modelling of step 1–3 is less important than assessing the mechanistic part of the model. However, trustworthiness of the results from the mechanistic model requires the statistical modelling to produce a reasonably good fit.

This chapter is organised as follows: Firstly, a number of figures are presented which serve to show what kind of spatial patterns the model produces. The idea is to give the reader a sense of the amount of migration which is necessary to mimic the real data fields. The general conclusion is that far from all BCBPs are migrating and they do not have to migrate very far in order to mimic real data. This provides a nice sanity check of the model, since we neither expect BCBPs to migrate large distances nor expect all BCBPs to migrate. Secondly, and most importantly, the results from the DRP analysis are presented. Finally, the results of the K function analysis are presented. The K function analysis is presented after the DRP analysis in order not to move focus away from the DRPs and over to the less interesting results of the statistical modelling. The fitting of the K functions is not perfect, and could be optimised in a separate study.

3.1 Optimal Parameters

The best parameters were identified by following the procedures sketched out in Section 2.5. Fitting the statistical model by adjusting the parameters μ_{BC}, σ_{BC}, d_{BC}^{min}, μ_{BCBP}, σ_{BCBP} and d_{BCBP}^{min} had to be done manually by

simply trying out different combinations of parameters. Not surprisingly, this proved to be a very time consuming exercise and it can be said with certainty that the *truly* optimal parameters have not been identified. It is difficult to conjecture about how far the identified parameters are from the truly optimal ones, and how large the implied discrepancy in the output is, but wide ranges of parameter values were evaluated and if some degree of continuity in the output is assumed, then it follows that the identified parameters probably do not perform much worse than the unknown truly optimal ones. For the future, research on optimising parameters, of the kind used here, in models of spatial point patterns is warranted.

The identified parameters are shown in Table 3.1. Remember that only one parameter, $\mu_{f/s}$, relates directly to the mechanistic part of the model (the interaction between BCs and BCBPs), the other six all relate to the statistical modelling of BCs and BCBPs.

3.2 Visual Comparison of Real and Simulated Data Fields

The immediate result of running the model is to obtain $N = 99$ simulations of each of the five fields. Presenting all 500 (496 simulated and 5 real) fields would be nonsensical, but it is instructive to show the five real fields as well as an example simulation of each of those. The plots are shown in Figure 3.1 on Page 36 (Fields 1–3) and in Figure 3.2 on Page 37 (Fields 4–5).

The first thing to notice is the significant difference in BC and BCBP densities across the five fields. This was already noted in Table 2.3. Next, the regularity of both BCs and BCBPs is clearly visible in both the real data fields and the simulated data fields. Given that only one simulated example is shown for each field, we do not expect it to be optimal, but it looks convincing.

Regarding the interaction between BCs and BCBPs, it is very hard to infer anything from a visual inspection of the plots. In the section on the DRP analysis below (Section 3.5), quantitative measures of this interaction will be presented.

3.3 Differentiation of Blue Cones

Given the end result of the model, illustrated in the previous section, it is time to have a look at the results from the different steps of the model. Firstly, the differentiation of BCs from progenitor cones was modelled as described in

	Monkey 1				
	Field 1	Field 2	Field 3	Field 4	Field 5
Mean BC exclusion zone, μ_{BC} (μm)	30	38	28	30	37
SD of BC exclusion zone, σ_{BC} (μm)	6	5.5	3	6	7
BC truncation, d_{BC}^{min} (μm)	13	32	18	18	23
Mean BCBP exclusion zone, μ_{BCBP} (μm)	18	18	18	19	22
SD of BCBP exclusion zone, σ_{BCBP} (μm)	5	6	5	3	7
BCBP truncation, d_{BCBP}^{min} (μm)	8	7	5	5	3
Mean relative friction/string force, $\mu_{f/s}$	0.75	0.90	0.82	0.84	0.97

Table 3.1: Parameters used in this study. The parameters shown were the best among the set of combinations of parameters, which was manually tried. Hence, they are unlikely to be truly optimal, but the error is probably not big enough to change the conclusions.

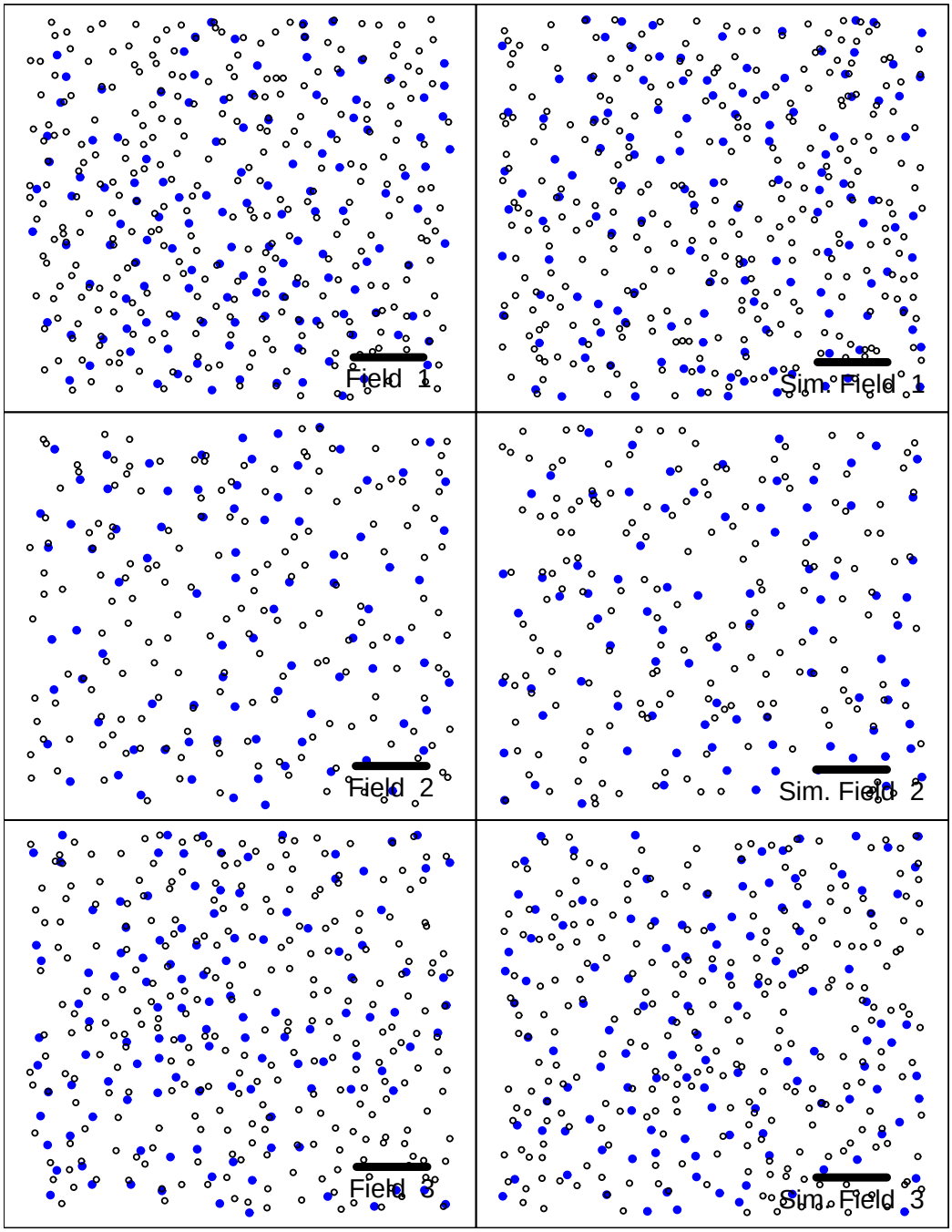

Figure 3.1: Fields 1–3. Visual comparison of the real data fields and the simulated fields. Fields in the left column are real data fields, and fields in the right column are examples of simulated data fields. Solid blue circles are BCs and open circles are BCBPs. The size of the circles relative to the size of the field corresponds to real physical size of BC and BCBP perikarya. Scale bar is 100 µm.

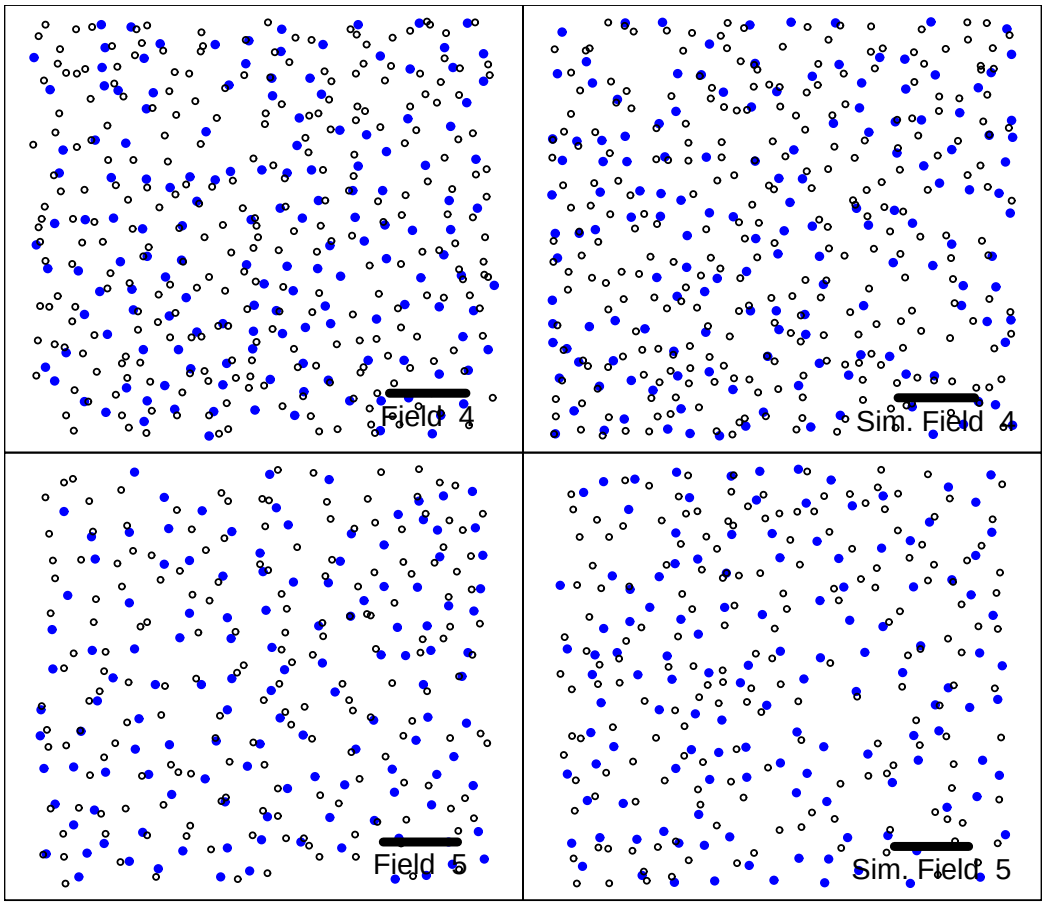

Figure 3.2: Fields 4–5. Same caption as for Figure 3.1.

Section 2.2 and an example simulation of field 1 is shown in Figure 3.3. The relative size of the circles in the figure are indicative of the real size of adult cones (diameter of approx. 10 µm [21]). This gives an impression of how densely retinal cones are packed. Rods (not simulated here) are interspersed between cones.

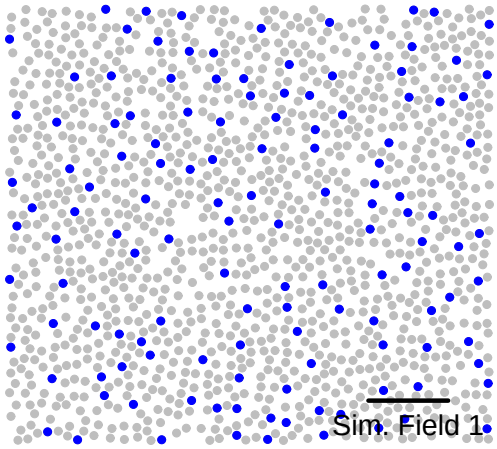

Figure 3.3: Example from the simulation of blue cones (blue circles) differentiating from cones (smaller filled black circles) in field 1. The size of the circles relative to the size of the field corresponds to real physical size of BCs. This gives an impression of how densely retinal cones are packed. Scale bar is 100 µm.

3.4 Blue Cone Bipolar Dendrites and Migration

The best way to get a sense of the effects of the mechanistic model is to consider the BCBP migrations that it causes. Hence, Figure 3.4 and 3.5 illustrate BCBP migration and dendritic contacts with BCs for fields 1–3 (Figure 3.4) and fields 4–5 (Figure 3.5). BCs are indicated as blue filled circles, BCBPs as open circles and the initial positions of those BCBPs that migrate are indicated as filled red circles. In the left column, BCBP migration is illustrated with dashed lines (between red circles and open circles). In the right column, postmigrational dendrites are illustrated with black lines and BCBP migration is illustrated with dotted lines. Again, the relative sizes are to scale.

It should be noted that most BCBPs do not migrate and that migration implies that BCBPs move closer to BCs (see Appendix A.1). Hence, dendritic length will decrease. Figure 3.6 shows the relation between dendritic length

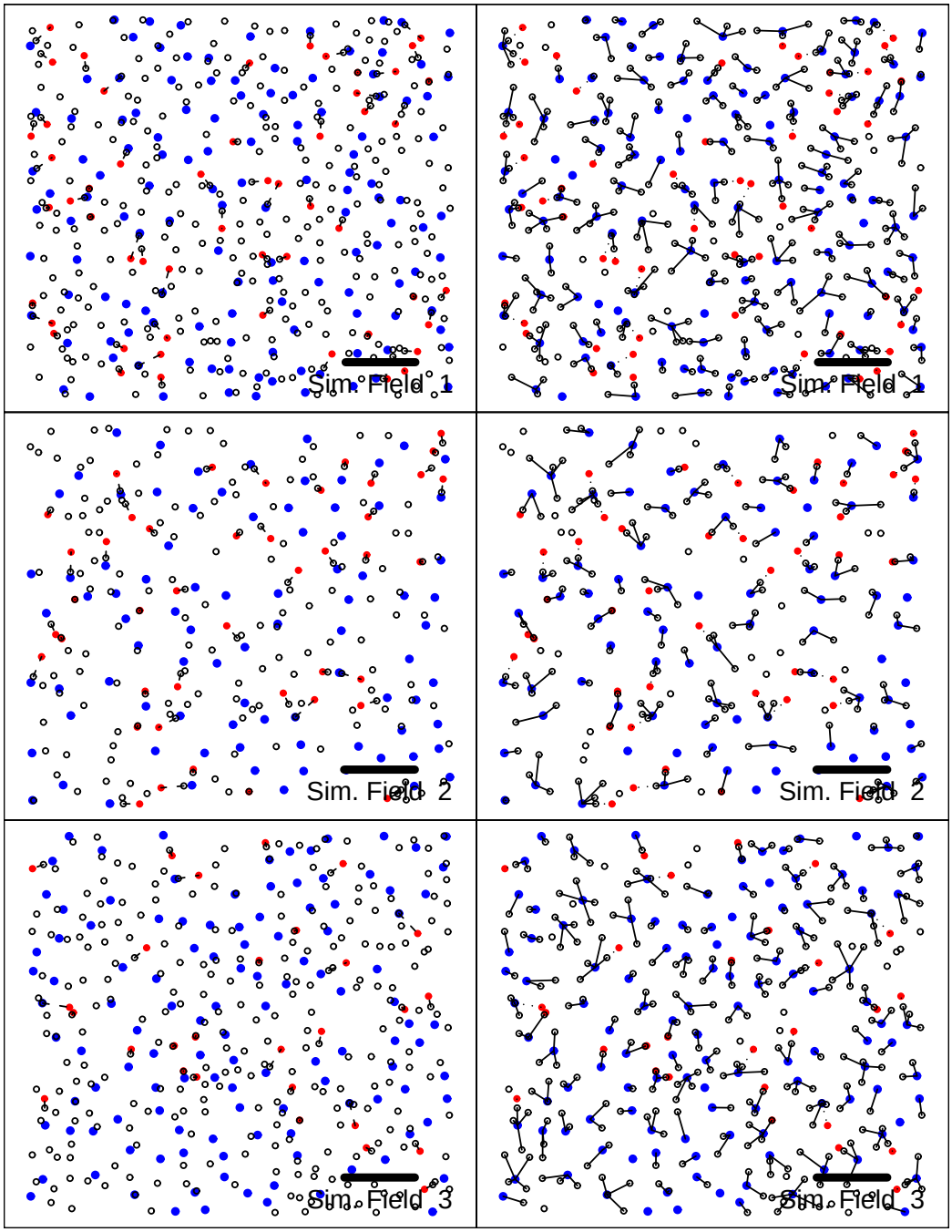

Figure 3.4: BCBP migration and dendritic contacts with BCs for field 1–3. BCs are indicated as blue filled circles, BCBPS as open circles and the initial positions of those BCBPs that migrate are indicated as filled red circles. In the left column, BCBP migration is illustrated with dashed lines (between red circles and open circles). In the right column, postmigrational dendrites are illustrated with black lines and BCBP migration is illustrated with dotted lines. Again, the relative sizes are to scale. Scale bar is 100 µm.

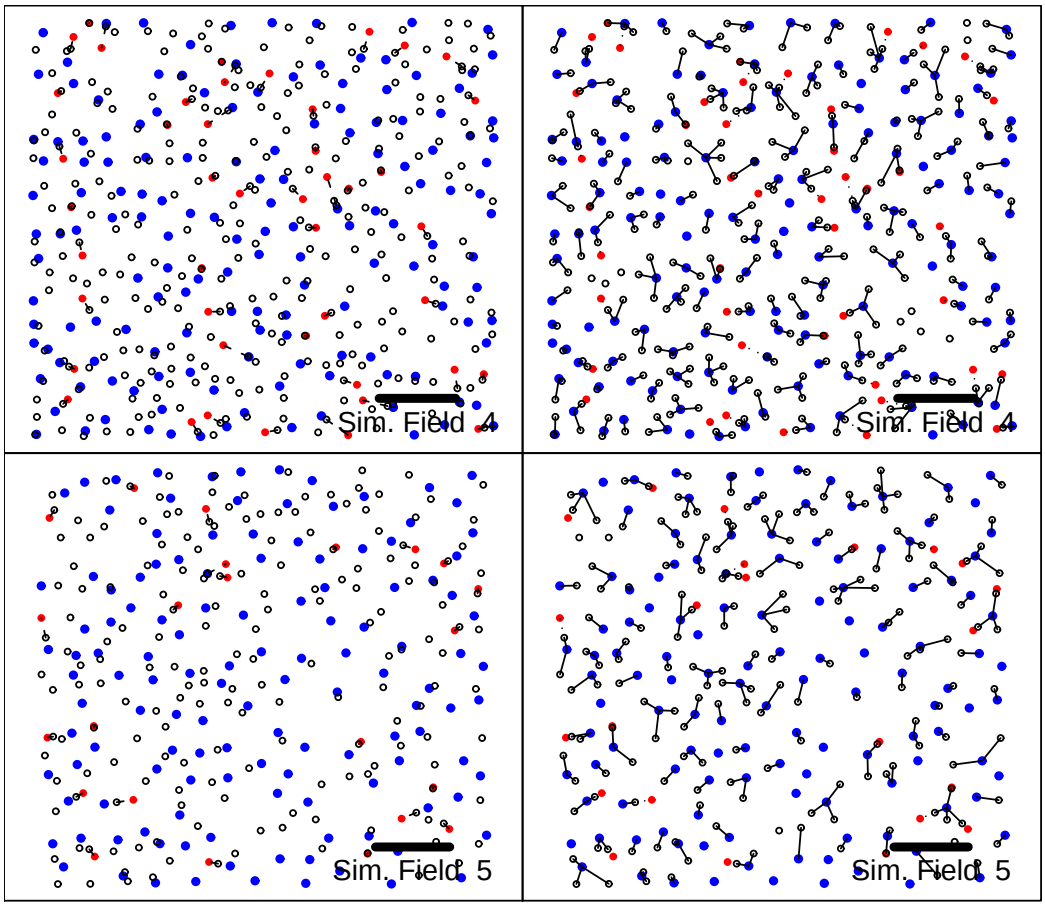

Figure 3.5: BCBP migration and dendritic contacts with BCs for field 4–5. The caption is the same as for Figure 3.4.

before and after BCBP migration (for one simulation). Several observations are of interest.

First of all, it is again seen that most BCBPs do not migrate (see also Figure 3.8 on Page 45 below for quantitative assessment of the proportion of migrated BCBPs). Secondly, BCBPs which are closer than $15 - 20\,\mu\text{m}$ (in the lateral plane) to their presynaptic BC pedicle do not migrate. This is a consequence of the mechanistic model. When the lateral distance between BC pedicle and BCBP is short, the projection of the string force becomes small and insufficient to overcome the friction force.

Thirdly, there is no clear relation between initial dendritic length l_0 and final dendritic length $|l^*|$[12]. Performing linear regression for each field in Figure 3.6, using only the BCBPs which have moved, gives p values of $p = (0.50, 0.37, 0.51, 0.83, 0.17)$ for the hypothesis of no explanatory power of the premigrational dendritic length l_0 on postmigrational dendritic length $|l^*|$.

In theory, there is a negative relationship between l_0 and $|l^*|$. This is shown formally in Appendix A.2, but the explanation is intuitive. If premigrational length is increased from some initial value l_0 to $l_0 + \delta l$ (and given the value of $F_{(f/s)}$), the BCBP (if it moves) will have a positive speed when it reaches the position l_0. Since the friction force is velocity independent, this implies that it will migrate further, the larger the premigrational length. This negative relationship is not seen in Figure 3.6 because $F_{(f/s)}$ varies between BCBPs and there are not enough BCBPs to produce a representative sample.

Now, Figure 3.6 only corresponds to a single simulation and is therefore not representative. Figure 3.7 illustrates the average dendritic length of all BCBPs before (black bars, $l_{0,\bullet\bullet}$) and after (grey bars, $l^*_{\bullet\bullet}$) BCBP migration. The average is both across BCBPs and the $N = 99$ simulations, i.e.

$$l_{0,\bullet\bullet} = \frac{1}{N n_{BCBP}} \sum_{j=1}^{N} \sum_{i=i}^{n_{BCBP}} l_{0,ij} \tag{3.1}$$

$$l^*_{\bullet\bullet} = \frac{1}{N n_{BCBP}} \sum_{j=1}^{N} \sum_{i=i}^{n_{BCBP}} l^*_{ij} \tag{3.2}$$

The dot notation for averages has been adopted. A dot in the place of a subscript indicates that this subscript has been averaged out.

[12]Lengths have to be positive. l_0 is positive by definition, whereas l^*, in theory, could be negative and therefore the length is $|l^*|$. For the values of $F_{(f/s)}$ and l_0 used in this study, however, l^* is positive, see Appendix A.1.

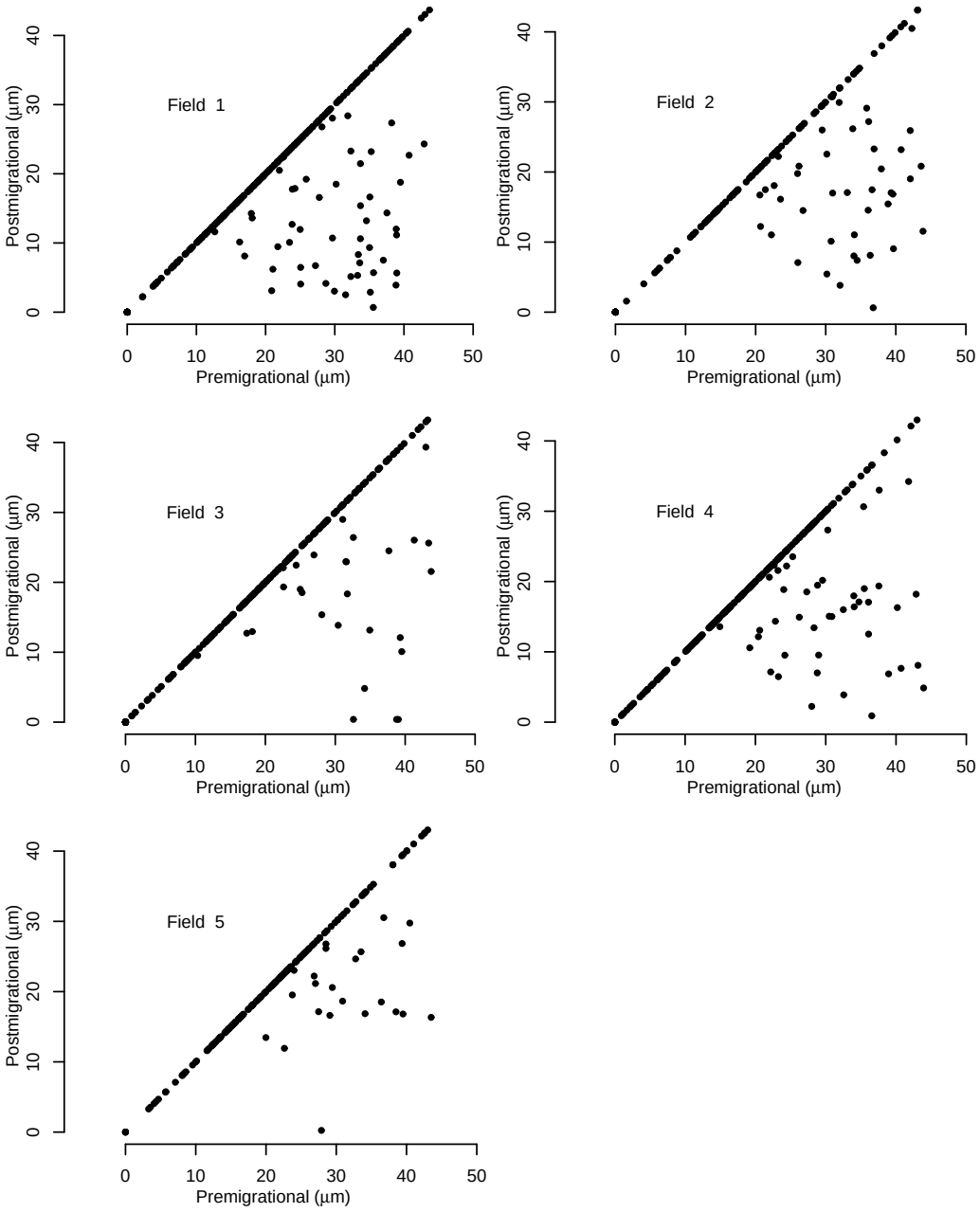

Figure 3.6: Plot of relation between postmigrational dendritic length $|l^*|$ and premigrational dendritic length l_0 for one example simulation for each of the five fields.

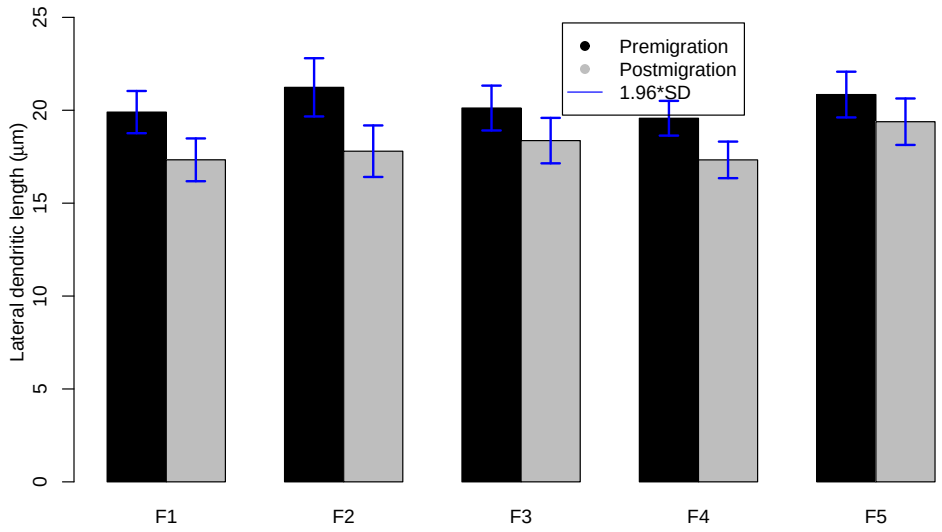

Figure 3.7: Pre- (black bars) and postmigrational (grey bars) dendritic lengths for all BCBPs for each field. Error bars indicate 1.96 times the standard deviation of the means of the simulations.

The error bars in Figure 3.7 are these averages $\pm$ 1.96 times the standard deviation of the means of the simulations, i.e. $l_{0,\bullet\bullet} \pm 1.96 \cdot sd(l_{0,\bullet j})$ and $l^*_{\bullet\bullet} \pm 1.96 \cdot sd(l^*_{\bullet j})$, respectively.

The average premigration values are around 20 µm, which can be explained as follows. The maximum dendritic length is $l_{\max} = 44$ µm and the premigration density of BCBPs around a BC grows with the square of the distance. This implies an average length of 33 µm (see Appendix A.3), but in this argument we have naively ignored that as the distance from the BC increases the chance that the BCBP will connect to another BC increases. This effect explains why the average premigrational dendritic length is around 20 µm and not around 33 µm as would naively be expected.

The postmigration values are averages of all BCBPs, also including those which do not move. The difference between pre- and postmigrational dendritic lengths is around 2-3 µm. For estimates of the migration distance for the BCBPs that actually migrate, see five paragraphs below and Figure 3.9.

Furthermore, the premigrational lengths are largest for field 2. This is caused by the lower density of BCs in this field. To understand this, note that if there are infinitely many BCs, the dendritic lengths would be $l_0 = 0$ for all BCBPs. Reducing the number of BCs, increases the distance to the nearest BC neighbour. Some BCBPs become too distant from BCs and will not even make a connection. This increase will only stop when there are so few (and regularly distributed) BCs that each BCBP can maximally reach only one BC. This point is not reached in the fields studied here. Hence, the lower the BC density, the larger the premigrational dendritic length.

It is tempting to reverse this argument and conclude that the fewer BCBPs the smaller l_0, but this is flawed since BCs and BCBPs are not symmetric. BCBPs can grow one dendrite which connects to a BC pedicle, whereas a BC pedicle can connect to several BCBP dendrites.

Based on Figure 3.4, 3.5 and 3.6 it was also mentioned that most BCBPs do not migrate. Figure 3.8 shows the mean and standard deviation (across simulations) of the proportion of BCBPs that move in each of the five fields. Only between 10 % and 20 % of BCBPs migrate. This is a nice result, since we do not expect all BCBPs to migrate and since it shows that far from all BCBPs need to migrate in order to produce the BC-BCBP interaction, which is seen in the real data.

Again, field 2 is exceptional. The low BC density in this field implies, as we have seen, that the dendrites tend to be longer, and this in turn implies that the projected string force will be stronger thus increasing the likelihood of migration.

It was also mentioned that migration distances were not very large because migrating BCBPs merely move closer to the nearest BC. Figure 3.9

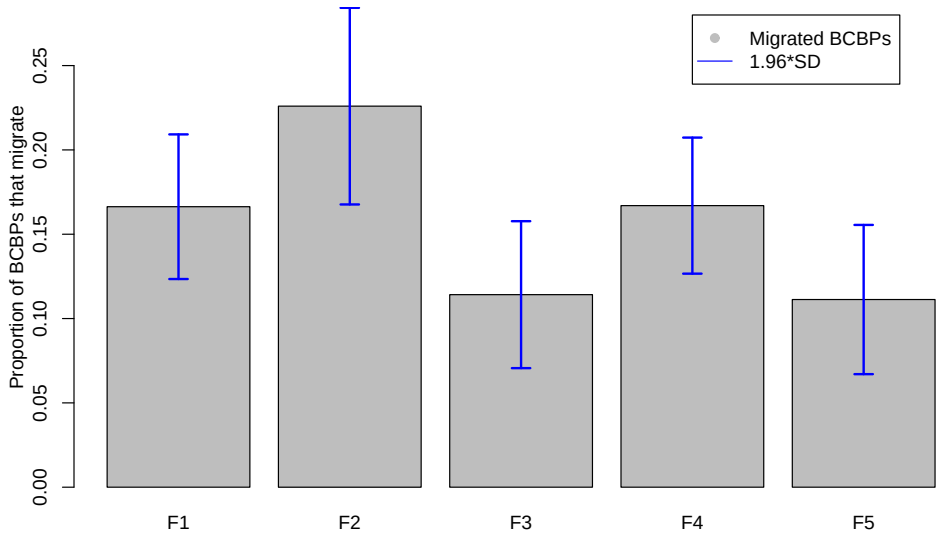

Figure 3.8: Proportion of BCBPs that migrate. Mean and standard deviation of $N = 99$ simulations of each of the five fields.

shows that migration distances average around 15 µm for all fields. The figure also emphasises that there is substantial variation in average migration distances between simulations.

Finally, the number of synapses in the simulated model can be compared with the real number of synapses. Remember that it was assumed that BCBPs either connect to zero or one BC. We know, that some BCBPs connect to two BCs (Figure 2.4 on Page 15). Hence, we would optimally expect that the simulations have generated less synapses than there are in the real data. Figure 3.10 shows that this is only the case for field 4 and 5. In the case of field 1–3, the simulated number of synapses is larger than the real data number. This implies that the simulations of field 1–3 might have a higher capability to create BC-BCBP interactions than the real data. If the number of synapses in field 1–3 were reduced, then the peaks in the cDRP would become less pronounced (given the relative friction force) and a smaller relative friction force would be needed to reproduce the sizes of the peaks observed in real data.

Alternatively, the distribution shown in Figure 2.4 could have been mimicked, but as discussed in Section 2.2.4, this introduces technical difficulties. These difficulties can be overcome, but it has not been pursued in this project.

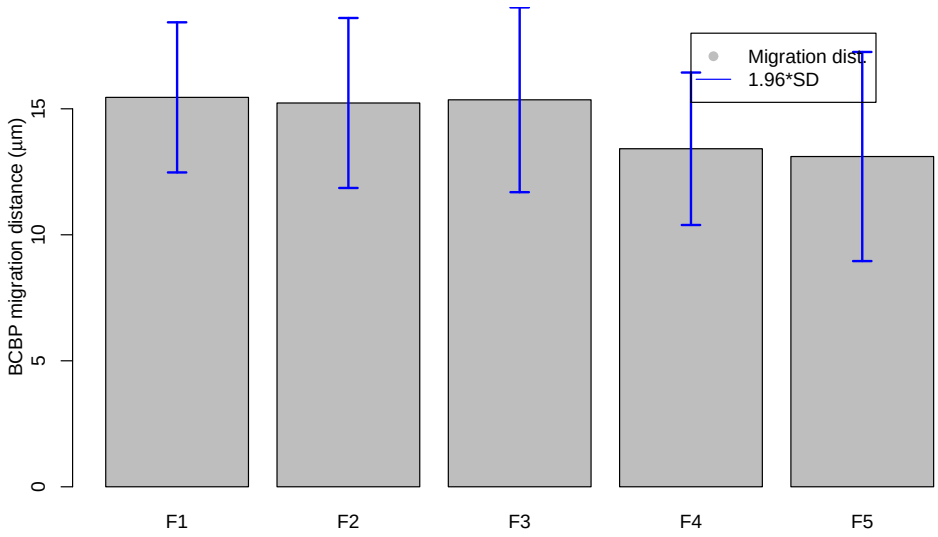

Figure 3.9: Migration distances. Mean and standard deviation of migration distances for $N = 99$ simulations of each of the five fields.

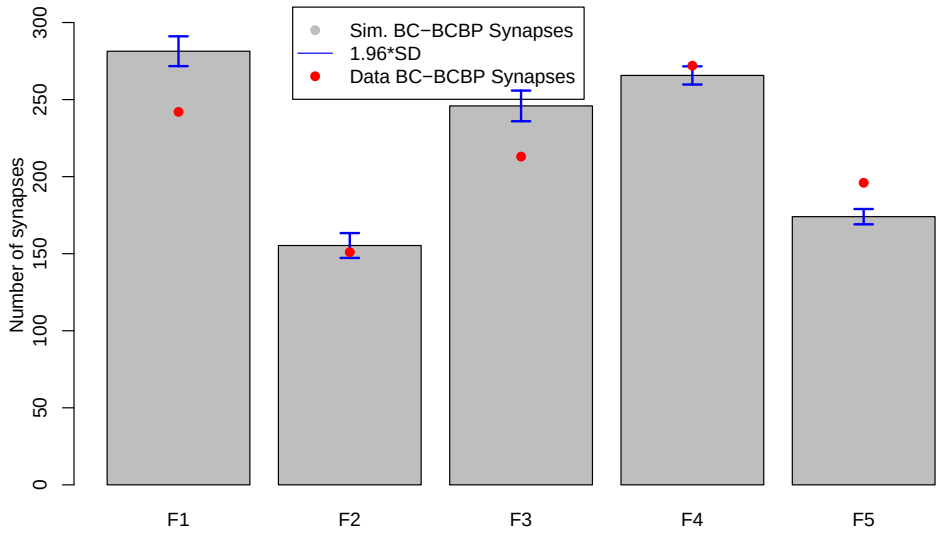

Figure 3.10: Number of synapses. Mean and standard deviation of the number of synapses for $N = 99$ simulations for each of the five fields. The number of synapses in the real data fields is indicated with red dots.

3.5 Density Recovery Profile Results

The DRP analysis is by far the most important analysis performed in this thesis, since this is the analysis which can potentially elucidate the interaction between BCs and BCBPs. The results are shown in Figures 3.11–3.15, one figure for each of the five fields. For each field, five different DRPs were generated. One aDRP for the BCs, two aDRPs for the BCBPs (before and after migration) and two bivariate cDRPs for the BC-BCBP interaction (before and after BCBP migration).

In the DRP figures, bars and error bars ($1.96 \cdot sd$) correspond to results of the simulations, and red dots correspond to real data. Note that there is no premigrational real data.

The general pattern should be quite clear from the figures. The BC DRPs all show a characteristic dip at small distances, which reflects the homotypic exclusion zone. At larger distances the DRPs 'recovers' to the macroscopic density (indicated by a horizontal line). The same is the case for the premigrational BCBP DRPs, with the difference that the exclusion zone is smaller and the macroscopic density is larger (see Table 2.3).

Comparing premigrational and postmigrational BCBP DRPs, it is seen that the postmigrational dip is smaller. This is essentially a consequence of the mechanistic model, BCs attract BCBPs, thereby bringing some BCBPs into close contact with each other (in the lateral plane).

The BC-BCBP cDRPs show that prior to BCBP migration, the two populations are uncorrelated (flat cDRP profile) as expected, but after BCBP migration, the two populations are correlated, which is seen from the fact that the postmigrational cDRP has the shape of a Mexican hat. BCs have attracted some BCBPs from their immediate vicinity, thereby creating a higher than average density for small distances ($< 20\,\mu\text{m}$) and lower than average density for distances up to around the maximal dendritic length of $l_{\max} = 44\,\mu\text{m}$.

Comparing the results of the Monte Carlo simulation (bars) with the real data (red dots) shows that, in general, there is a good fit. In the case of the BC aDRP and the BCBP aDRP these results are not groundbreaking, given that the parameters of the model were chosen in order to secure a reasonable fit. However, the cDRPs are very interesting. The real data results are almost always within the error bars of the simulated results and the shape of the simulated cDRPs closely follows the shape of the real data cDRPs.

This shows that the mechanistic model is capable of reproducing the interactions between BCs and BCBPs observed in the real data. This does not prove the model right, but it corroborates the underlying assumptions.

Of course, these results depend on the choice of the relative friction-

to-string force (see Table 3.1) and indeed the relative flat cDRP for field 5 was the result of a mean relative force of $\mu_{f/s} = 0.97$, somewhat larger than the mean relative forces for the other fields (see Table 3.1). Field 2 is the exception to this rule. Here, $\mu_{f/s} = 0.90$, which is much higher than for field 1 ($\mu_{f/s} = 0.75$) but despite this, the relative sizes of the peaks of those two fields are similar. Hence, field 2 is intrinsically more capable of attracting BCBPs to BCs and a higher friction force is needed to inhibit this mechanism. This can probably be explained by the fact that the density of BCs and BCBPs are lower in field 2 and thus the BCBPs can migrate more freely towards the BC with less risk of colliding with other BCBPs.

Finally, it should be mentioned that the reason the error bars tend to get smaller with increasing distance is very simple. As distance increases, the area increases quadratically and thus there are many more cells at a distance of, say, 80 μm from a reference cell than cells at a distance of, say, 10 μm.

3.6 Regularity Index and Density Recovery Profiles Statistics

Based on the DRPs, a number of quantitative measures can be calculated that summarises each field. Yet another measure is the regularity index, which is based on nearest neighbour distances. These were all discussed in Section 2.3. The results are printed in Table 3.2. The table includes the effective radius r_{eff}, the maximum radius $r_{\max}$, the packing factor p, the macroscopic density D and the regularity index RI.

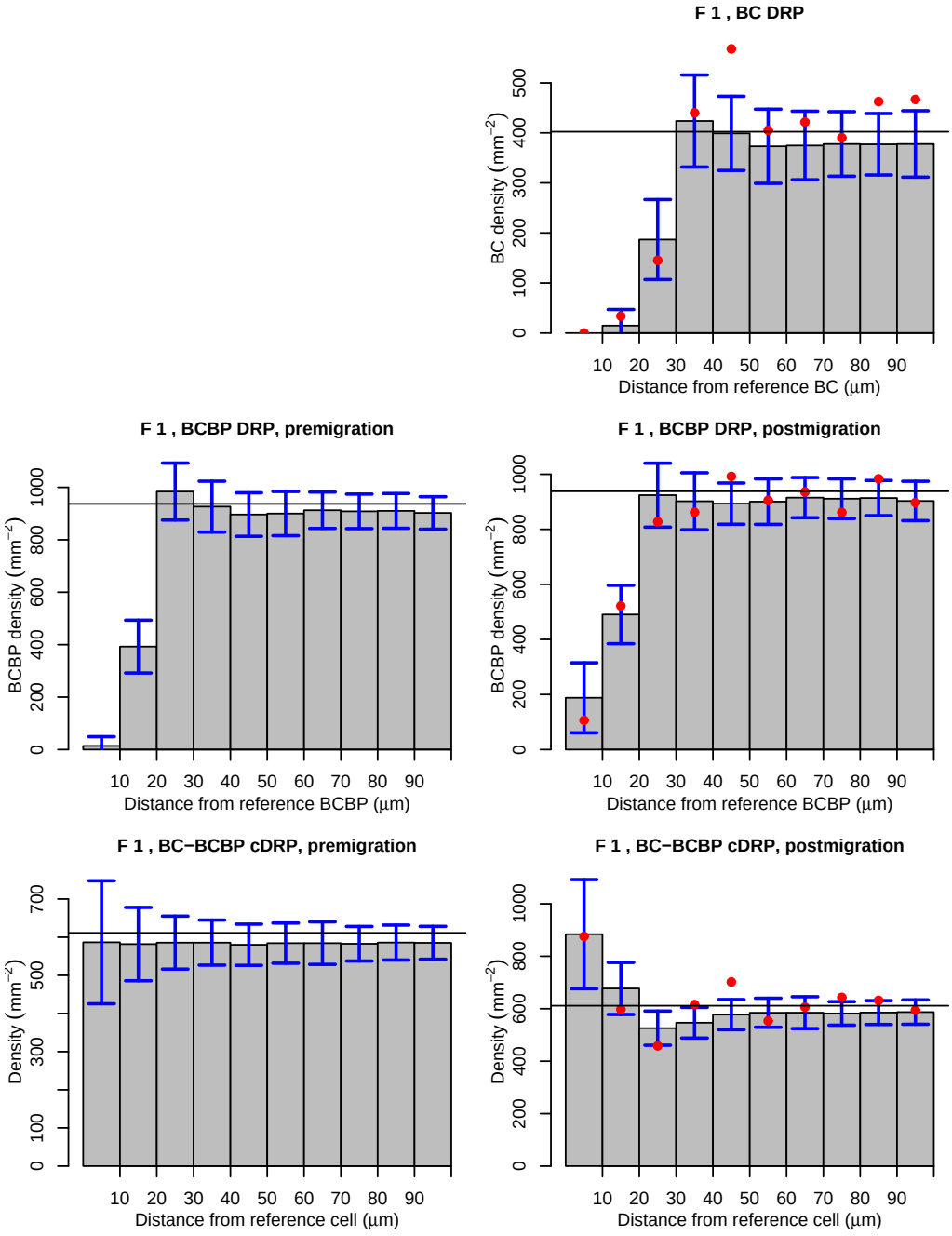

Figure 3.11: DRP results for field 1. Bars indicate mean of $N = 99$ simulations, error bars indicate 1.96 standard deviations of these simulations, red dots indicate real data results and horizontal line indicates macroscopic density. The dip in the BC and BCBP DRP reflects the homotypic exclusion zones. Postmigrationally, the BCBP dip becomes smaller because of migration towards BCs, since this implies that some BCBP will cluster around BCs. Premigrationally, the cDRP is flat, indicating independence between BCs and BCBPs, but postmigrationally, there is a significant peak at small distance, indicating that BCs have attracted BCBPs and that the two populations are correlated.

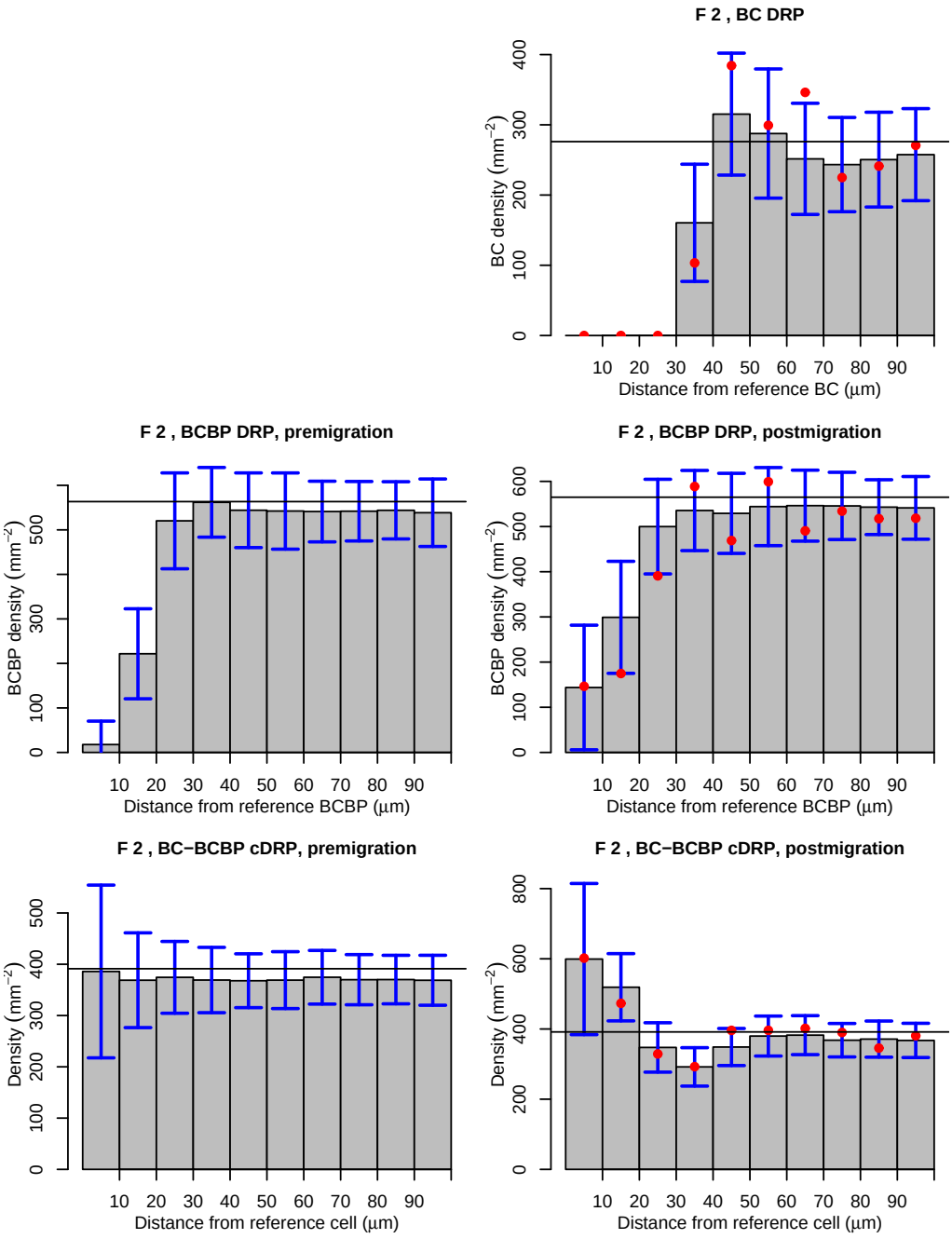

Figure 3.12: DRP results for field 2. Same caption as for 3.11.

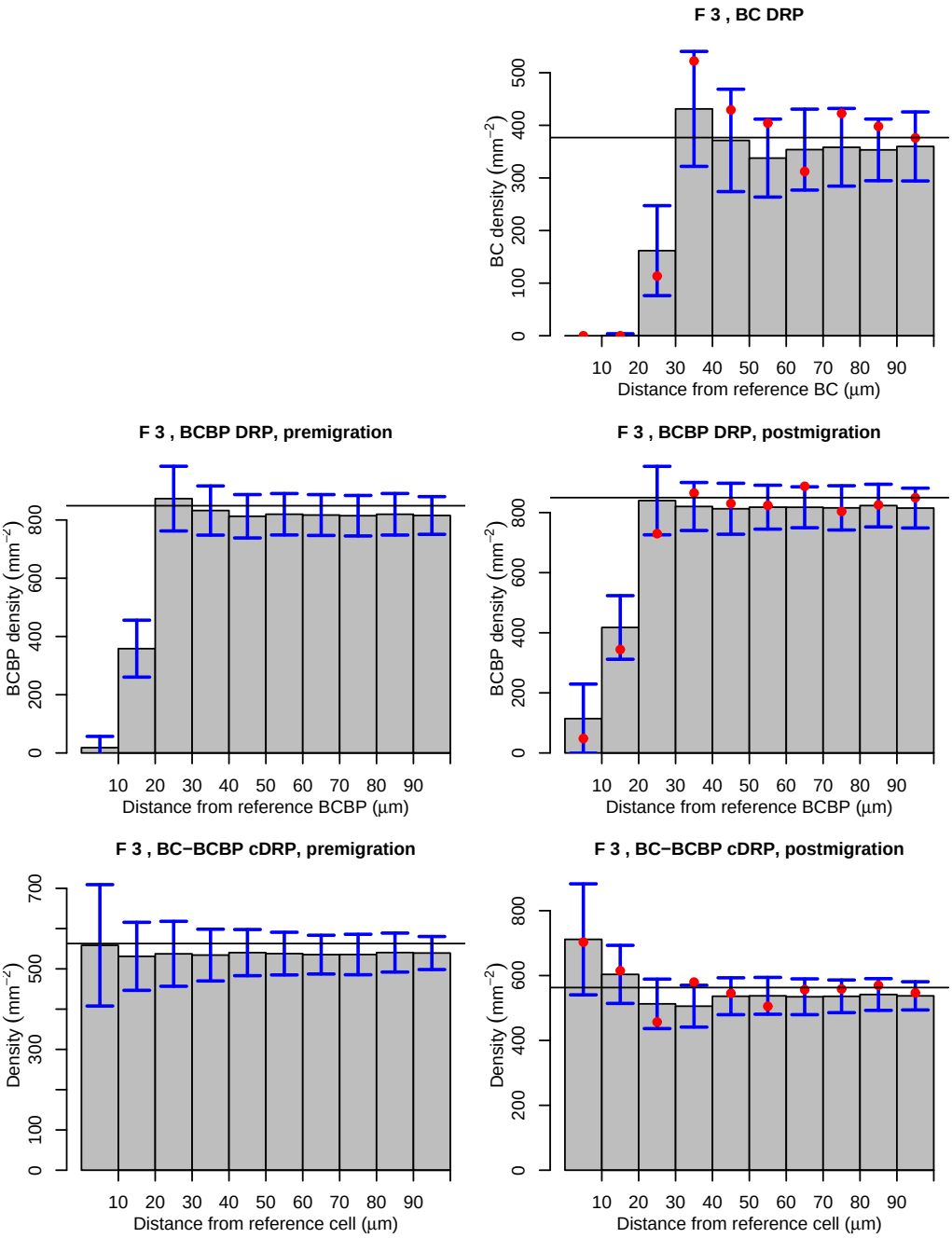

Figure 3.13: DRP results for field 3. Same caption as for 3.11.

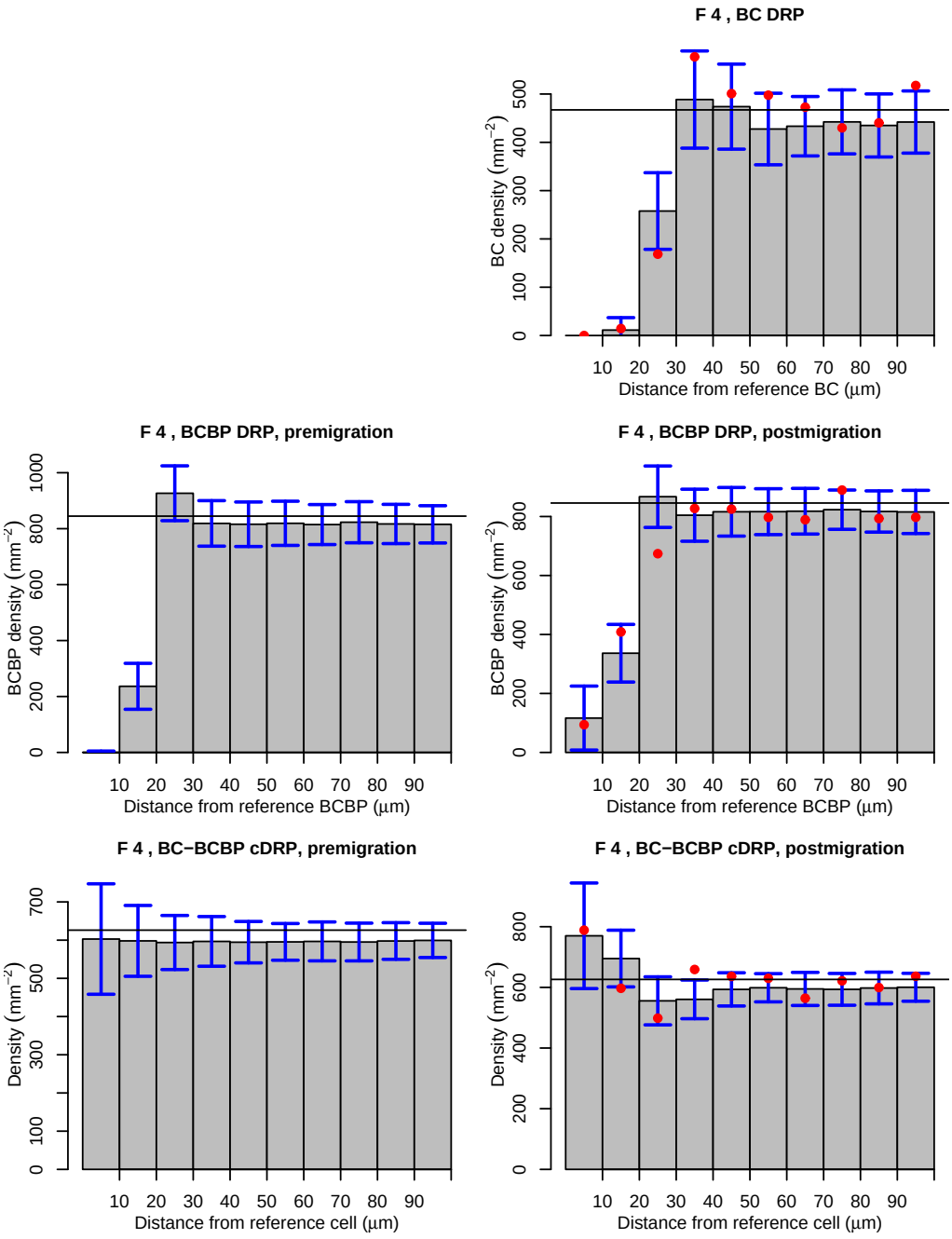

Figure 3.14: DRP results for field 4. Same caption as for 3.11.

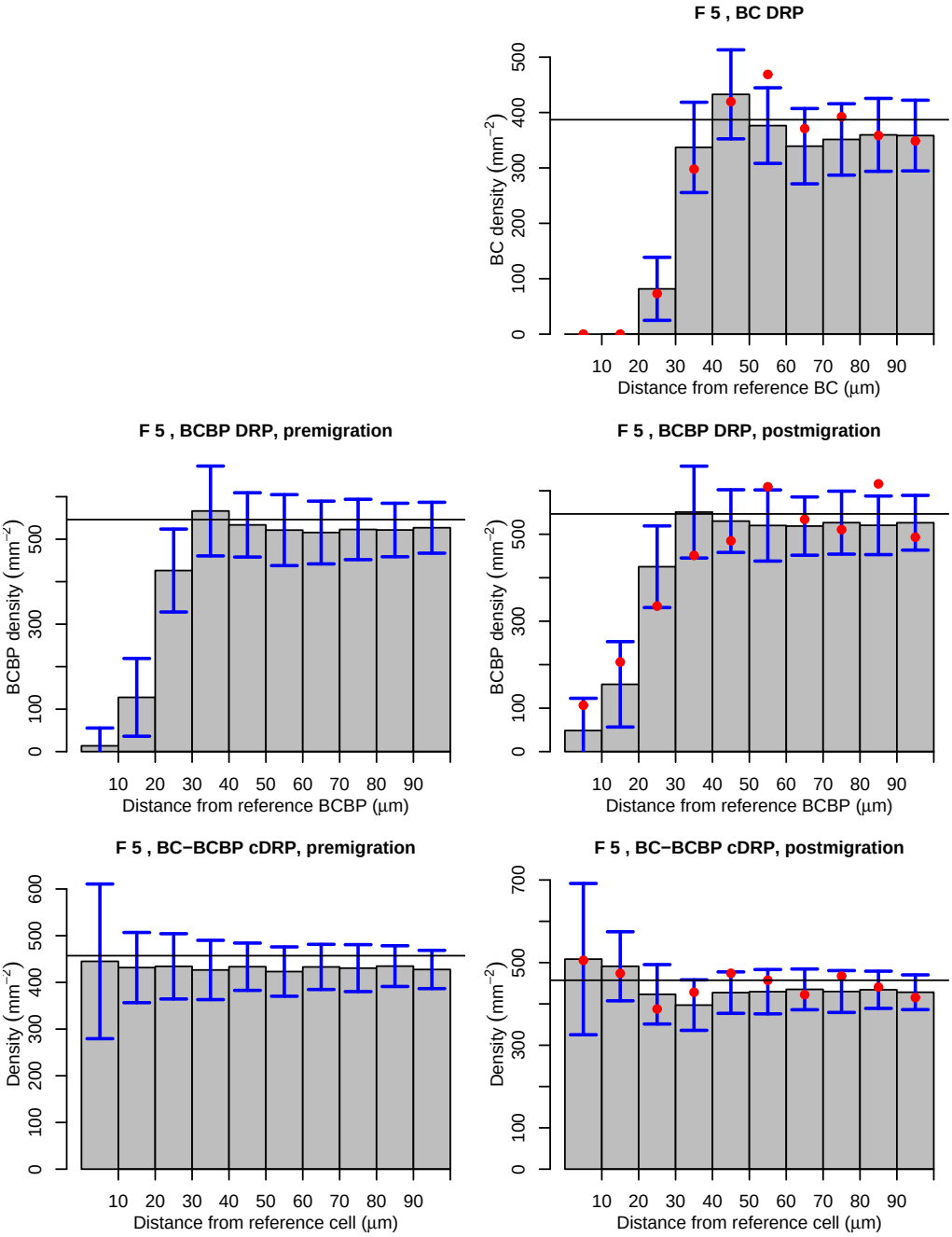

Figure 3.15: DRP results for field 5. Same caption as for 3.11.

	r_{eff} (µm)			$r_{\max}$ (µm)			p			D (mm^{-2})			RI		
	μ	σ	data	μ	σ	data	μ	σ	data	μ	σ	data	μ	σ	data
F1, BC	26.41†	(1.90)	26.4	53.6	(0.15)	53.4	0.24†	(0.04)	0.24	402	(2.26)	406	4.11	(0.32)	4.76
F1, BCBPb	16.61	(0.57)	-	35.1	(0.06)	-	0.22	(0.02)	-	937	(3.19)	-	3.99	(0.27)	-
F1, BCBPa	16.91	(2.26)	18.2	35.1	(0.07)	35.2	0.24	(0.07)	0.27	938	(3.94)	933	3.15	(0.18)	3.26
F1, BCBCBPb	3.58	(4.77)	-	43.5	(0.04)	-	0.02	(0.04)	-	611	(1.21)	-	-	(-)	-
F1, BCBCBPa	0.02	(0.21)	0.0	43.5	(0.05)	43.5	0.00	(0.00)	0.00	611	(1.43)	609	-	(-)	-
F2, BC	34.75	(1.62)	36.6	64.7	(0.27)	64.4	0.29	(0.03)	0.32	276	(2.31)	279	5.21	(0.53)	6.04
F2, BCBPb	19.24	(2.89)	-	45.3	(0.17)	-	0.18	(0.06)	-	563	(4.38)	-	3.16	(0.25)	-
F2, BCBPa	20.04†	(4.11)	20.7	45.2	(0.19)	45.4	0.2†	(0.09)	0.21	565	(4.80)	559	2.66	(0.24)	2.86
F2, BCBCBPb	4.27	(5.56)	-	54.3	(0.09)	-	0.02	(0.03)	-	391	(1.32)	-	-	(-)	-
F2, BCBCBPa	0.00	(0.00)	0.0	54.3	(0.10)	54.6	0.00	(0.00)	0.00	392	(1.48)	388	-	(-)	-
F3, BC	26.38	(1.11)	27.4	55.4†	(0.18)	55.3	0.23	(0.02)	0.24	377†	(2.41)	377	4.34	(0.43)	5.47
F3, BCBPb	17.23	(1.96)	-	36.9	(0.07)	-	0.22	(0.06)	-	849	(3.46)	-	3.77	(0.22)	-
F3, BCBPa	17.76	(2.88)	18.5	36.9†	(0.09)	36.9	0.24†	(0.08)	0.25	850†	(4.01)	850	3.22†	(0.22)	3.25
F3, BCBCBPb	3.99	(5.07)	-	45.3	(0.04)	-	0.02	(0.04)	-	563	(1.12)	-	-	(-)	-
F3, BCBCBPa	0.13	(0.57)	0.0	45.3	(0.05)	45.4	0.00	(0.00)	0.00	563	(1.20)	561	-	(-)	-
F4, BC	25.42	(1.4)	26.7	49.7	(0.06)	49.7	0.26	(0.03)	0.29	467	(1.20)	468	4.50	(0.35)	4.74
F4, BCBPb	17.89	(0.61)	-	37.0	(0.07)	-	0.23	(0.02)	-	845	(3.27)	-	4.50	(0.26)	-
F4, BCBPa	17.17	(1.72)	23.1	36.9†	(0.08)	36.9	0.22	(0.05)	0.39	846†	(3.72)	846	3.43	(0.25)	3.06
F4, BCBCBPb	4.56	(5.17)	-	42.9	(0.03)	-	0.03	(0.05)	-	626	(0.80)	-	-	(-)	-
F4, BCBCBPa	0.13	(0.62)	0.0	42.9	(0.03)	43.0	0.00	(0.00)	0.00	626	(0.87)	624	-	(-)	-
F5, BC	29.97	(1.31)	31.3	54.6	(0.10)	54.2	0.30	(0.03)	0.33	387	(1.41)	394	4.93	(0.47)	4.79
F5, BCBPb	21.54	(1.68)	-	46.0	(0.15)	-	0.22	(0.04)	-	546	(3.56)	-	3.56	(0.32)	-
F5, BCBPa	21.77	(2.79)	25.8	46.0	(0.15)	46.2	0.23	(0.07)	0.31	547	(3.56)	541	3.26	(0.31)	2.79
F5, BCBCBPb	4.38	(5.73)	-	50.3	(0.06)	-	0.02	(0.04)	-	457	(1.12)	-	-	(-)	-
F5, BCBCBPa	0.96	(1.75)	0.0	50.3	(0.06)	50.4	0.00	(0.00)	0.00	457	(1.12)	455	-	(-)	-

Table 3.2: Statistics based on the DRP analysis (r_{eff}, $r_{\max}$, p and D) and the regularity index (RI) have been calculated for the simulated data and for the real data. For the simulated data, standard deviations across simulations have also been calculated. These statistics have been calculated for each of the five DRPs (BC, BCBP before migration, BCBP after migration, BC-BCBP before migration and BC-BCBP after migration). The first column of each statistic contains the mean of the simulated values, the second column contains the standard deviation of the simulated values and the third column contains the real data value. 'b' indicates before migration and 'a' indicates after migration. † means that a standard t-test yields no significant difference between the mean of the simulated values and the real data value.

In Chapter 2, it was described how simple t-tests can be used to test whether there is a significant difference between real data and simulated data. We do not expect the difference between simulated results and real data results to be statistically insignificant, but we do expect it to be numerically small. This is generally seen to be the case. In a few cases, the differences are even insignificant, these cases are marked with an asterisk[13].

It should be noted that there is generally a slight difference between the macroscopic densities of the real data fields and the simulated fields. This must be caused by slight differences between the real data areas and the simulated data areas[14]

3.7 Testing Hypotheses

Hypothesis 1 within DRP framework First, it was considered whether entire DRPs could be considered flat, i.e. random/independent. Not surprisingly, it was found that in isolation BCs, premigrational BCBPs and postmigrational BCBPs are not randomly distributed across the fields (all p values were zero).

In the case of independence between BCs and BCBPs, it was found that after migration they were dependent. Again, this is hardly surprising, the correlation between BCs and BCBPs is the subject of this thesis!

Prior to BCBP migration, we would expect BCs and BCBPs to be independent. Considering the roughly flat cDRP plots it seems plausible. However, a closer inspection of these plots reveals that in the case of F2, F3 and F5, the first bin is slightly higher than the others. It does not seem as much and these bins also have larger error bars, but it is sufficient to reject the hypothesis that BCs and premigrational BCBPs are independent (at a 5% level), $p = (0.98, 0.04, 0.00, 0.89, 0.01)$. If we discard the first bin, there is no correlation between BCs and BCBPs, $p = (0.98, 0.91, 0.74, 0.99, 0.39)$. Since the BCs and BCBPs are generated independently, we know that the cDRP should be flat. The slightly higher first bin must merely be a result of smaller sample size, and therefore larger variation, in this region.

Next, the dependence between BCs and BCBPs was also examined by testing if the postmigrational cDRP densities were significantly different from

[13] It is easy to see which ones are significantly different, since the standard deviation of the mean is simply the standard deviation divided by the square root of the number of observations, i.e. approximately 10.

[14] Remember from Section 2.2.1 that in the simulations, the dimensions of the fields were determined as the ranges L_x and L_y in the x and y dimension, respectively, of the cells in the real fields. Kouyama and Marshak [1] might have defined the fields slightly differently.

premigrational densities. t-tests were used as described in Section 2.4. In general, these tests showed that for bins with a distance larger than 40 μm, there was no significant difference between pre- and postmigrational cDRP. For bins with a distance smaller than 40 μm, there was a significant difference. This again shows how the string forces work within a distance of $l_{\max} = 44\,\mu\text{m}$. The exception to this was field 2, where the seven first bins were significantly different, i.e. up to 70 μm.

Finally, testing whether the pre- and postmigrational BCBP DRPs were identical, bin by bin, showed that for bins with a distance greater than 40μm, there were no significant changes. This was expected.

Test of hypothesis 2 in DRP framework All of the DRP plots shown above are significantly different from data, all p values are practically zero. This is hardly surprising considering that the data points in the DRP plots fluctuate somewhat around the bars. With $N = 99$ replications, this amount of fluctuation is sufficient to reject hypotheses about identity of real data and simulated data. However, looking at individual bins instead of entire DRP plots, some bins are not significantly different from their data counterpart. As a rule of thumb, if the red dot is closer than one tenth of the length of an error bar to the grey bar, then there is no significant difference between real data and simulated data.

Test of hypothesis 3 in DRP framework It is not surprising that no pair of DRP plots from two different fields can be considered identical, even after normalising DRPs with field specific macroscopic densities. After all, the five fields are taken from different parts of the retina, and no one expects the retina to be spatially homogeneous.

At this point it is worth noting that Kouyama and Marshak [1] concluded that the five real data fields could be merged. I think, however, that this conclusion is wrong. Kouyama and Marshak used a model for the heights of the bins similar to the model applied but here, but since they only have one observation of each bin, they cannot estimate all interaction terms α_{ij}. Instead they considered the model $y_{ij} = \beta_i + \gamma_j + \epsilon_{ij}$, where β_i is the effect of field i and γ_j is the effect of bin j. They normalised the bin heights y_{ij} by the macroscopic densities, thereby effectively eliminating β_i. Hence, it is not surprising that they accepted the hypothesis of identical field effects, $\beta_1 = \ldots = \beta_5$.

3.8 K Functions

K functions were used to assess the goodness of fit of second-order properties between the simulated and the real data. K functions were calculated for BCs, BCBPs and for the BC-BCBP interaction. Given the relatively simple statistical modelling of BC and BCBP generation, we do not expect the K function fits to be very accurate. In this thesis, however, focus is mainly on the mechanistic model. Hence, obtaining very good fits from the statistical modelling is not crucial.

In the case of CSR, $K(t) = \pi t^2$ and thus $L(t) \equiv \sqrt{K(t)/\pi} = t$. Hence, it is easier to detect departures from CSR if the L function is plotted instead of the K function.

Figure 3.16 shows L functions for all five fields (rows) and for BCs (first column), BCBPs (second column) and the interaction between BCs and BCBPs (third column). Real data L functions are drawn with blue lines, and the 95 % envelope of simulations are indicated with red lines. The dashed line is $L(t) = t$ and is added in order to compare with CSR. The diagram below each plot shows the magnitude of T_i with T_1 highlighted in blue. Remember, that T_1 is the test statistic for comparing real data with the simulated data. If this value is in the extreme upper end of the T_i distribution, then there is a significant difference between data and simulation. The p values indicated in the plots are simply the relative rank (decreasing order) of T_1 among T_i.

In general, the simulated envelopes contain the real data and only in a few cases do real data L functions 'leave' the envelopes. Given this, it might be surprising that some p values are insignificant. This is because p values are based on a comparison of the real data with the mean of the simulated data. If the real data L function does not fall in the centre of the envelope, this will reduce the p value. Also, some envelopes are very narrow, which means that obtaining a large p value is very demanding. For example, $L_{BC,BCBP}$ for field 1 has a $p = 0.01$, despite the fact that the blue line is never far away from the centre of the envelope.

Turning attention away from general observations and looking closer at individual p values, it is noticed that fields 2, 4 and 5 have good fits, whereas fields 1 and 3 are more troublesome. For these two fields, it proved very hard to generate BC mosaics which resembled real data (p values of 0.03 and 0.00, respectively). The reason is easily identified by looking at the blue L_{BC} lines. In the case of field 1 and 3, there is a pronounced kink (this is hard to see in Figure 3.16, therefore Figure 3.17 shows L_{BC} for field 1 and 3 more clearly). The statistical model (exclusion zones drawn from a truncated Gaussian) that generated BC mosaics was too simplistic to mimic this pattern. A more sophisticated model with more parameters could have been devised, but this

was not done for two reasons. (i) Anything can be fitted if the number of parameters is sufficiently high and (ii) it is not very critical that these fits are not perfect since the main focus of the project was to study the mechanistic model.

The BCBPs of fields 1 and 3 were similar to the other fields and the p values are quite good. The p values for the BC-BCBP interaction of fields 1 and 3 are very different, $p = 0.01$ and $p = 0.59$, respectively. It might seem counterintuitive that the p value for field 3 is so high given the poor fit of the BCs, but this is perfectly possible since the interaction between BCs and BCBPs is not dependent on the BC mosaic. As mentioned in the introduction, there has even been found a BC-BCBP interaction in the New World monkey marmoset, where the BCs are completely random [11].

Finally, it might also seem surprising that the L function curves for the BC-BCBP interaction follow the 45° line so closely. Does this mean that BCs and BCBPs are uncorrelated, and would this not be at odds with the results from the DRP analysis? The answer is simply that Figure 3.16 is not suitable for detecting departures from the 45° line. The last panel in Figure 3.17 shows a zoom of $L_{BC,BCBP}$ for field 1. From this it is clear that there is a departure from the 45° line and therefore from CSR.

As mentioned in Chapter 2, a complement to the K function is the G function, which is a cumulative measure of nearest neighbour distances. G functions have been calculated and the results were similar to the K function results in the sense that a good fit for an L function also implied a good fit for a G function. Therefore, plots of G functions have not been included in this thesis.

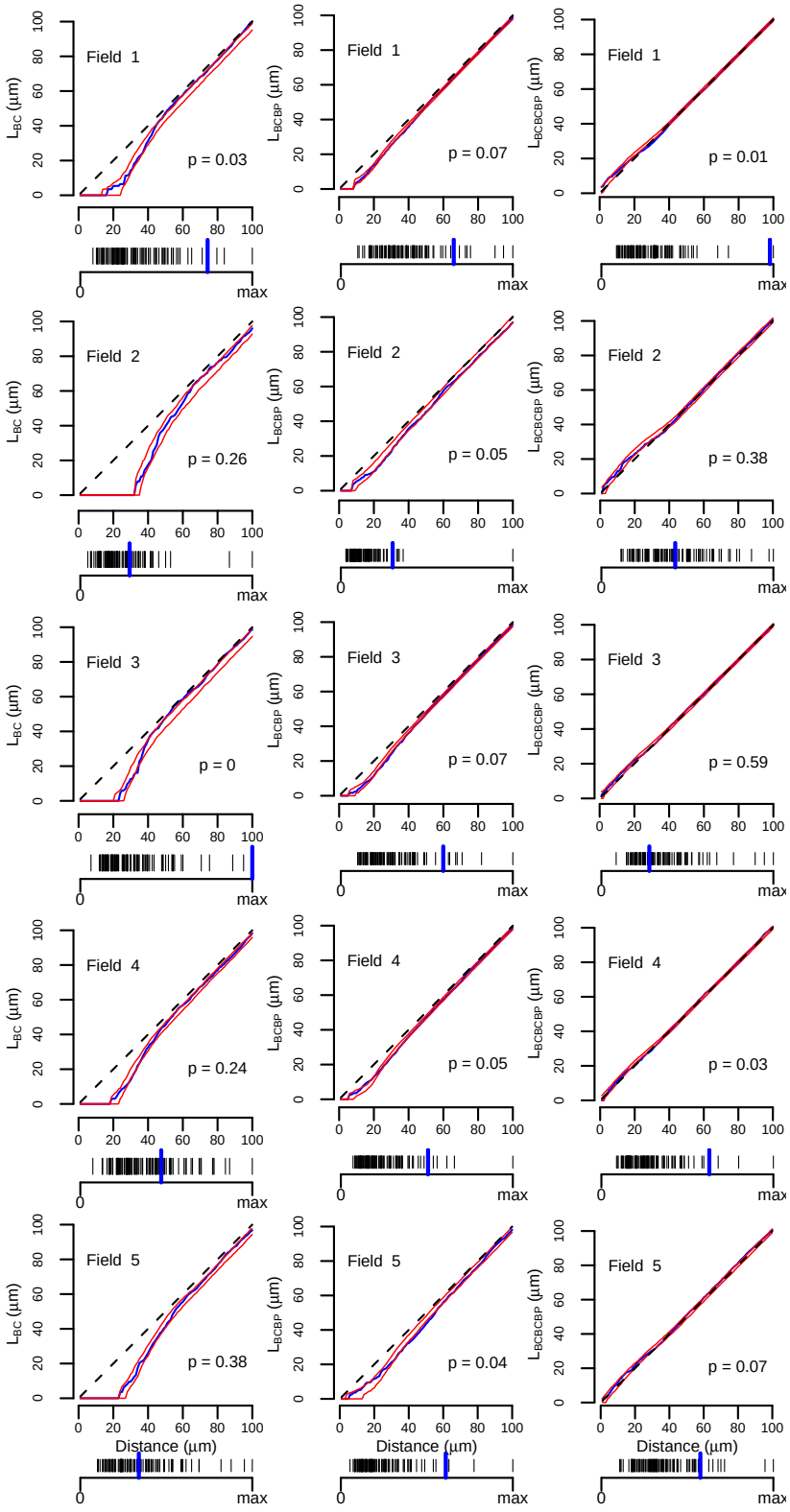

Figure 3.16: L functions. The figure shows L functions for each combination of field (rows) and cell populations (columns). The first column contains BC L functions, the second contains BCBP L functions and the third contains BC-BCBP L functions. Blue lines indicate real data L functions, red lines indicate 95 % envelopes of simulated L functions. Dotted lines indicate 45 degree lines, which correspond to CSR in the univariate case and to independence in the bivariate case. Below each plot, the ranking of T^1 is shown (see Section 2.4), which corresponds to the p values shown in the plots.

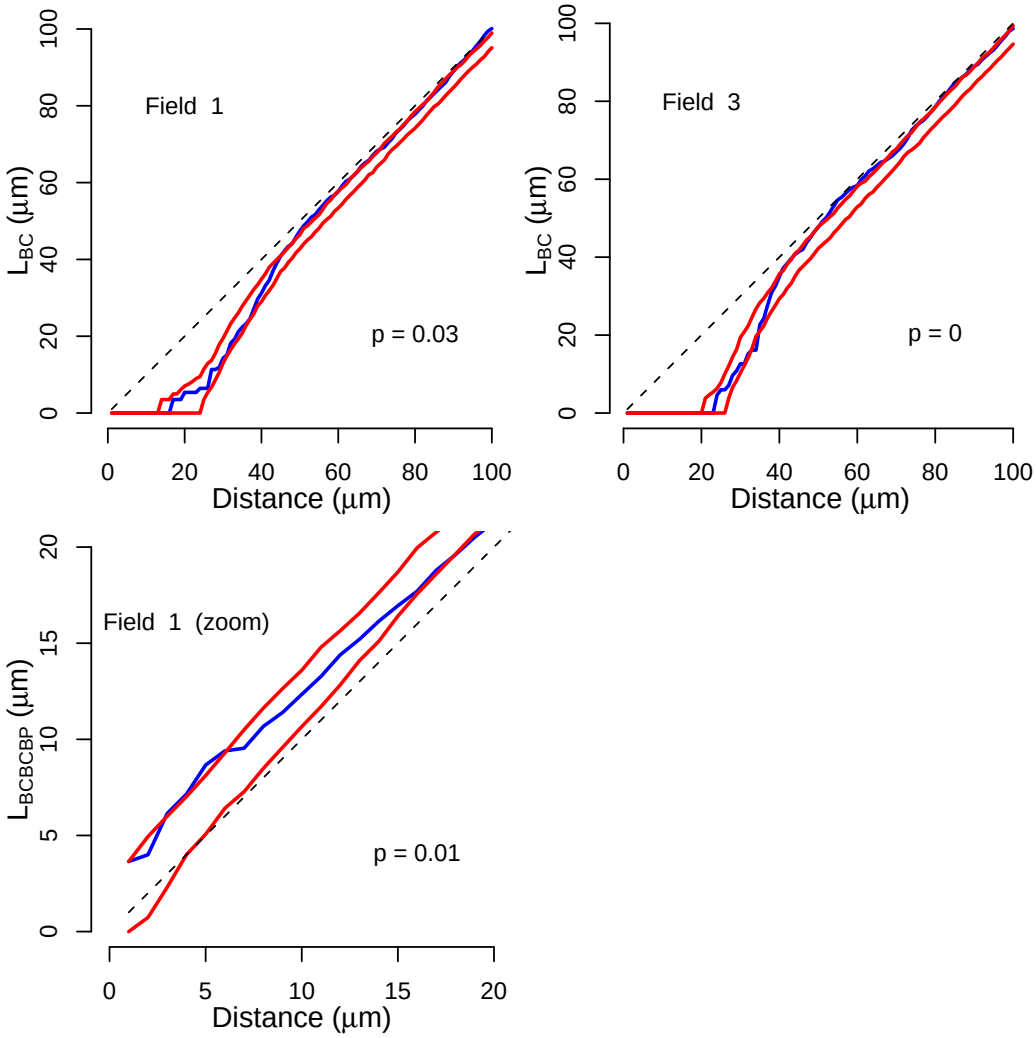

Figure 3.17: L_{BC} for field 1 and 3 and a zoom of $L_{BC,BCBP}$ for field 1. In this figure, the kinks in L_{BC} for field 1 and 3 are more visible than in Figure 3.16 and the departure from the 45° line for $L_{BC,BCBP}$ is also much more visible than in Figure 3.16.

Chapter 4

Discussion and Conclusion

The ultimate ambition of studying retinal mosaics is to reveal the mechanism that drives the pattern formation. In this thesis, a mechanistic model for the interaction between BCs and BCBPs has been developed, simulated and assessed. The cornerstone of the model is that a BCBP can migrate due to a compromise between a string-like force exerted by the dendrite, connecting the BCBP with a BC, and friction force in the INL.

Using DRP analysis, it has been showed that the mechanistic model is capable of reproducing the empirically observed pattern of BC-BCBP interactions. This qualifies the model as a candidate model for the mechanism that generates the BC-BCBP correlation.

Other candidate models have been described in the literature. It has been suggested that a BC and a BCBP are daughters from a common progenitor cell [43], i.e. they were born at the same place and have mainly migrated radially. This hypothesis, however, fits badly with the DRP results which shows that the correlation is far from perfect. At least this hypothesis should be supplemented by some explanation of why the BCs and BCBPs are not perfectly correlated. Also, as pointed out by Kouyama and Marshak [1], the fact that some BCBPs make two dendritic contacts seems to be at odds with the idea that they only contact sister BCs.

These considerations led Kouyama and Marshak to favour an explanation based on dendritic interactions and relative migration of BCs and BCBPs. They did not, however, develop an explicit model of this interaction. This gap has now been filled.

Another interesting empirical observation, which is in accordance with the model, is the fact that in marmoset (a New World monkey) BCs and BCBPs are positioned randomly in the ONL and INL, respectively, but conditional on the positions of BCs, the BCBPs are nonrandom. In other words, BCs and BCBPs are also correlated in marmoset, but this correlation does not rely

on BC or BCBP mosaics. This is in accordance with the model developed here: the BCs are 'leaders' and via dendritic interactions with BCBPs, they induce BCBPs to migrate, i.e. to become 'followers'.

Another piece of information that supports this idea of 'leaders' and 'followers' is the fact that bipolar cells differentiate after cone photoreceptors [4, Chap. 3]. Hence, at the time of presumptive BCBP migration, the BCBPs may be more flexible and mobile than BCs, which is exactly what has been assumed in this thesis. BCBPs could therefore be thought of as 'add-ons', which adjust to the already established BC array. Evolutionary, bipolars also developed after cone photoreceptors, so this is an example of the general idea that what came later in evolution also comes later in the development of the individual organism [44].

Finally, in a study by Reese *et al.* [45] it has been found that a number of cell types migrate less then 100 μm. In the framework of the model developed in this thesis, the migration of BCBPs can conceptually be decomposed into two parts: (i) migration caused by dendritic interactions with BCs and (ii) migration before a dendritic connection to a BC is made. A sanity check on the model developed here, is that it should not predict migration distances above 100μm. According to the output from the model developed here, migration caused by dendritic interactions is around 15 μm.

Based on these considerations, it is fair to say that the model developed in this thesis should be considered in future experimental and theoretical work on the developing retina.

Suggested future research based on the model developed here can be divided into two groups, theoretical and experimental. First, more theoretical work could be carried out. For example, Kouyama and Marshak [1] describes sixth data fields, but only five of these have been used in this project. One way of using the last data field would be to estimate the model based on a part of this sixth field and then to test the model on another part of this sixth field (the sixth field is four times larger and more dense than the fields used here). This, obviously requires that these two parts of the sixth field has the same macroscopic density.

Another idea for future theoretical work is to conduct a sensitivity analysis of the parameters of the model, particularly on the relative friction-to-string force. Information about the sensitivity of the output with respect to the relative force would be valuable for future experimental work.

On the experimental side, techniques for measuring cellular forces are now available (optical tweezers) and measurements of dendritic string forces and retinal friction forces would obviously provide a test of this model. In general, future experiments could provide a test of the assumptions made in this model. With a mechanistic model, testable hypotheses emerge much

more naturally than with a statistical model, and this is a strong argument for mechanistic models. Some assumptions could prove wrong and should be discarded, some might need an adjustment and some might be perfectly supported by experiments. In this manner, future experiments could spur new theoretical ideas which then could be built into future mechanistic models of the BC-BCBP interaction. In other words, there is still a lot of work to be done.

Appendix A

Derivations and Proofs

A.1 Postmigrational Blue Cone Bipolar Position, Eq. (2.1)

The cornerstone of the mechanistic model is the migration caused by the dendritic string force. In Chapter 2, the formula describing the postmigrational BCBP position was merely stated (Eq. 2.1) without derivation. This appendix presents the derivation.

BCBP migration is a linear motion and parallel with the INL. Thus, we only need to consider motion in one dimension. The physical situation is sketched in Figure A.1.

Let $\mathbf{F}_s$ denote the dendritic string force exerted on the BCBP. Assume that the BC pedicle is immobile[15] and that the BCBP can only move in a planar region and that the distance between the BC pedicle and this plane is d^v. In this plane, orient an axis starting from the projection of the BC pedicle and pointing in the direction of the BCBP. Let l denote the position of the BCBP on this axis, i.e. $|l|$ is the lateral distance between the BC pedicle and the BCBP. Let θ denote the angle which the connecting line between the BCBP and the BC pedicle forms with the l axis. Then the projection $\tilde{\mathbf{F}}_s$ on the BCBP plane of the dendritic string force $\mathbf{F}_s$ has length $\tilde{F}_s$ given by.

$$\tilde{F}_s = \cos\theta\,|\mathbf{F}_s| = \frac{l}{\sqrt{l^2 + (d^v)^2}} F_s. \tag{A.1}$$

Within the INL, the BCBP cannot move freely, it is subject to a friction force. It is assumed that the static and dynamic friction forces are identical

[15] If the BC pedicle is also allowed to move, the force exerted on the BCBP will not only depend on BCBP position but also on BC position, and vice versa. Hence, the equations of motion would become coupled differential equations, which it is nice to avoid.

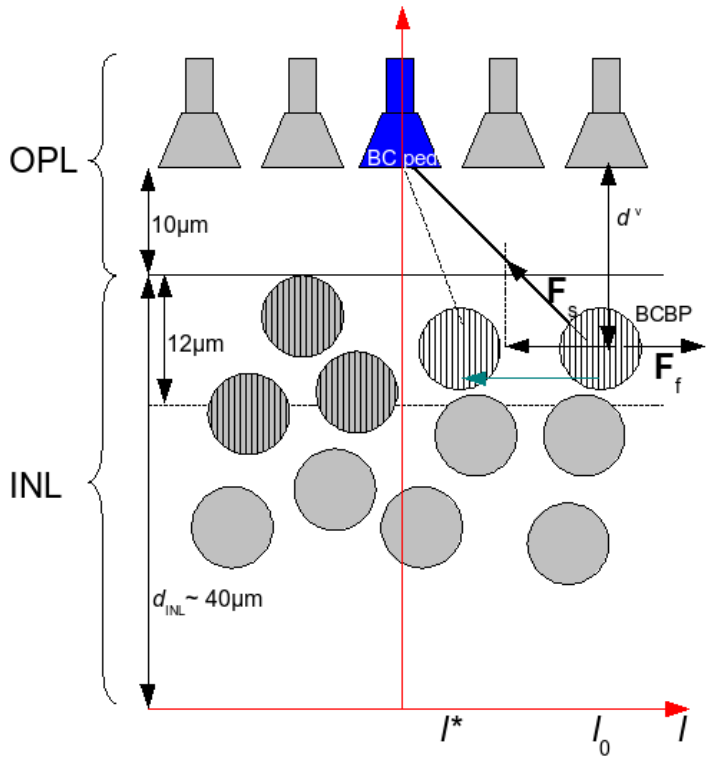

Figure A.1: Diagram of the mechanistic model. BC pedicles are fixed in the OPL, whereas BCBPs which are less than $3 \cdot r_{BCBP} = 12\,\mu m$ from the INL-OPL interface can migrate laterally within the INL. BCBPs are distributed in the INL with mean distance from the INL-OPL interface of a third of the INL depth and with a standard deviation of 0.11 of the INL depth. This implies that 38 % of BCBPs have the potential to migrate. The relative number of BCs and BCBPs, the radial distribution of BCBPs and the size of BCBPs match the real retina. BCBPs which are located deeper in the INL are assumed to be immobile because their dendrites will potentially not contact a BC pedicle in a straight line because of other BCBPs blocking the way. BCBPs which can potentially migrate have been hatched in the diagram, and BCBPs which cannot migrate are unhatched. An example of a BCBP migration is shown. The hatched BCBP with white background is connected with the blue BC pedicle. The BCBP is under influence of string force $\mathbf{F}_s$ and friction force $\mathbf{F}_f$. These forces are indicated with black arrows. The projection $\tilde{\mathbf{F}}_s$ of $\mathbf{F}_s$ on the lateral plane is also indicated with an arrow. The BCBP migrates from initial position l_0 to postmigrational position l^*. The turquoise arrow indicates the migration. The dashed line indicates the postmigrational dendrite. Red arrows indicate the coordinate axes. Relevant depth variables and magnitudes are indicated.

and have magnitude F_f. They are obviously directed in the opposite direction of $\tilde{\mathbf{F}}_s$. We shall assume that $\tilde{F}_s > F_f$ such that there will be motion. This assumption is immaterial, since the case of no motion is trivial.

Given this geometry, the equation of motion of the system reads

$$m\frac{d^2l}{dt^2} = F_f - \tilde{F}_s = F_f - \frac{l}{\sqrt{l^2 + (d^v)^2}}F_s, \tag{A.2}$$

where m is the mass of the BCBP[16]. If we let v denote the velocity, the second derivative on the left hand side of this equation can be rewritten as

$$\frac{d^2l}{dt^2} = \frac{dv}{dt} = \frac{dv}{dl}\frac{dl}{dt} = \frac{dv}{dl}v.$$

Dividing Eq. (A.2) by m and using the last expression we obtain

$$v\frac{dv}{dl} = \frac{F_f}{m} - \frac{F_s}{m}\frac{l}{\sqrt{l^2 + (d^v)^2}}.$$

In this expression it is possible to separate the variables v and l. Hence,

$$\int v\,dv = \int \left(\frac{F_f}{m} - \frac{F_s}{m}\frac{l}{\sqrt{l^2 + (d^v)^2}}\right) dl. \tag{A.3}$$

Performing the integration yields

$$\frac{1}{2}v^2 = \frac{F_f}{m}l - \frac{F_s}{m}\sqrt{l^2 + (d^v)^2} + C.$$

In order to determine C we can use that at $t = 0$, $l = l_0$ (initial position) and $v = 0$. Inserting this into the above equation yields

$$C = \frac{F_s}{m}\sqrt{l_0^2 + (d^v)^2} - \frac{F_f}{m}l_0. \tag{A.4}$$

The equation governing the relation between position l and velocity v is therefore

$$\frac{1}{2}v^2 = \frac{F_f}{m}l - \frac{F_s}{m}\sqrt{l^2 + (d^v)^2} + \frac{F_s}{m}\sqrt{l_0^2 + (d^v)^2} - \frac{F_f}{m}l_0. \tag{A.5}$$

[16]From this expression it is seen why a velocity dependent friction force is not appropriate. Assume that the friction force had the form $F_f = a + bv$. Solving the system requires us to find l such that $v = 0$ and $\ddot{l} = 0$. This implies that $l^* = \frac{d^v a/F_s}{\sqrt{1-(a/F_s)^2}}$, i.e. postmigrational dendritic length l^* is independent of premigrationel dendritic length l_0.

Now, we wish to determine the positions l where $v = 0$. We know that initially there will be motion (we assumed $\tilde{F}_s > F_f$). Because of the presence of friction, this motion cannot continue forever, eventually it will slow down and make $v = 0$, which means that either the BCBP has come to a stop or it is merely changing direction of motion. The latter can only be the case if $l < 0$, since only in this case can there be a force which will increase l. In this case, there will be oscillations. Because of the friction force, however, such oscillations will necessarily be damped, and therefore there will be at least one more l for which $v = 0$.

To conclude, if there is only one l, except for l_0, for which $v = 0$, then we know that also $\ddot{l} = 0$ and that the BCBP does not move anymore.

Imposing $v = 0$ in Eq. (A.5) and rearranging terms yields

$$F_f l + F_s\sqrt{l_0^2 + (d^v)^2} - F_f l_0 = F_s\sqrt{l^2 + (d^v)^2}.$$

This can be rewritten as a quadratic equation in l, and therefore it can have a maximum of two solutions. The quadratic equation reads

$$al^2 + bl + c = 0, \tag{A.6}$$

where

$$\begin{aligned} a &= F_f^2 - F_s^2 \\ b &= 2F_f\left(F_s\sqrt{l_0^2 + (d^v)^2} - F_f l_0\right) \\ c &= \left(F_s\sqrt{l_0^2 + (d^v)^2} - F_f l_0\right)^2 - F_s^2(d^v)^2. \end{aligned}$$

Note that $a \neq 0$, again because of the assumption that $\tilde{F}_s > F_f$, so this equation will never collapse into a linear equation.

After some tedious algebra, the discriminant of the quadratic Eq. (A.6) can be written as

$$d = 4F_s^2\left(F_f\sqrt{l_0^2 + (d^v)^2} - F_s l_0\right)^2 \geq 0,$$

which is seen to be non-negative. It is only 0 in the case of $F_f\sqrt{l_0^2 + (d^v)^2} = F_s l_0$, in which case there will be no motion. But this is assumed not to be the case, again by the assumption $\tilde{F}_s > F_f$. Hence $d > 0$ and there are two different real solutions, of which $l = l_0$ must be one. The solutions are

$$l^* = \frac{-b \pm \sqrt{d}}{2a} = \begin{cases} \frac{l_0}{\frac{2F_{(f/s)}\sqrt{l_0^2+(d^v)^2}-\left(F_{(f/s)}^2+1\right)}{1-F_{(f/s)}^2}} \end{cases}, \tag{A.7}$$

where we have introduced the shorter notation $F_{(f/s)} = F_f/F_s$. Note that the denominator is always positive.

A.2 Proof that $\frac{\partial|l^*|}{\partial l_0} < 0$

It will be shown that the postmigrational dendritic length $|l^*|$ decreases with premigrational length l_0.

First, we calculate the partial derivative of l^* with respect to l_0 from Eq. (A.7).

$$\frac{\partial l^*}{\partial l_0} = \left(\frac{1}{1-F_{(f/s)}^2}\right)\left[\frac{2F_{(f/s)}l_0}{\sqrt{l_0^2+(d^v)^2}} - \left(F_{(f/s)}^2+1\right)\right]. \tag{A.8}$$

Imposing the notational simplification $\alpha = \frac{2F_{(f/s)}l_0}{\sqrt{l_0^2+(d^v)^2}}$, this simplifies to

$$\frac{\partial l^*}{\partial l_0} \propto 2\alpha F_{(f/s)} - \left(F_{(f/s)}^2+1\right).$$

This is a second order polynomial in $F_{(f/s)}$ with discriminant $\tilde{d} = 4(\alpha^2-1)$. Since, by definition, $\alpha < 1$, it follows that $\tilde{d} < 0$ and the polynomial has no roots. Hence, $\frac{\partial l^*}{\partial l_0}$ is either positive or negative, but since $\left.\frac{\partial l^*}{\partial l_0}\right|_{F=0} < 0$ it follows that

$$\frac{\partial l^*}{\partial l_0} < 0.$$

Now this does not imply that the postmigrational dendritic length is a decreasing function of premigrational dendritic length. Postmigrational dendritic length is not l^* but instead $|l^*|$. In general it holds that

$$\frac{\partial|l^*|}{\partial l_0} = \begin{cases} \frac{\partial l^*}{\partial l_0} & \text{for } l^* \geq 0 \\ -\frac{\partial l^*}{\partial l_0} & \text{for } l^* < 0. \end{cases}$$

Hence, we need to know the signs of l^*. Based on the expression for l^* in Eq. (A.7) it follows that

$$l^* \geq 0 \text{ when } l_0 \leq \frac{2F_{(f/s)}}{|F_{(f/s)}^2-1|}d^v \tag{A.9}$$

$$l^* < 0 \text{ when } l_0 > \frac{2F_{(f/s)}}{|F_{(f/s)}^2-1|}d^v, \tag{A.10}$$

where it has been used that $F_{(f/s)} \neq 1$ (see Appendix A.1). We can therefore write

$$\begin{aligned} \frac{\partial |l^*|}{\partial l_0} &< 0 \quad \text{for } l_0 \leq \frac{2F_{(f/s)}}{|F_{(f/s)}^2 - 1|} d^v \\ \frac{\partial |l^*|}{\partial l_0} &> 0 \quad \text{for } l_0 > \frac{2F_{(f/s)}}{|F_{(f/s)}^2 - 1|} d^v. \end{aligned} \tag{A.11}$$

A typical value for $F_{(f/s)}$ is 0.9, which implies that $\frac{2F_{(f/s)}}{|F_{(f/s)}^2 - 1|} d^v \approx 10 d^v$. In turn, d^v is almost certainly larger than 10 µm. Lateral dendritic lengths l are never larger than 44 µm (see Subsection 2.2.4 in Chapter 2). We can therefore conclude that the migrating BCBPs will not be able to migrate beyond the projection of the BC pedicle and therefore $\frac{\partial |l^*|}{\partial l_0} < 0$.

A.3 Calculation of Mean Premigrational Dendritic Length

Prior to BCBP migration, BCs and BCBPs are spatially independent. We now consider a BCBP known to be migrating and thus known to be located within $l_{\max}$ of a given BC. Assuming that we know that this BCBP connects to this particular BC, the expected premigrational dendritic length is given by $\int_0^{l_{\max}} l\rho(l)\, dl$, where $\rho(l)$ is the density of BCBPs at a distance l from the BC. Because of the spatial independence between BCs and BCBPs, $\rho(l) = Al^2$. It also holds that $\int_0^{l_{\max}} \rho(l)\, dl = 1$. We can therefore calculate A

$$\int_0^{l_{\max}} \rho(l)\, dl = A \int_0^{l_{\max}} l^2\, dl = \frac{1}{3} A l_{\max}^3 = 1 \quad \Leftrightarrow \quad A = \frac{3}{l_{\max}^3}. \tag{A.12}$$

The expectation of l can now be expressed in terms of $l_{\max}$.

$$\langle l \rangle = \int_0^{l_{\max}} l\rho(l)\, dl = A \int_0^{l_{\max}} l^3\, dl = \frac{3}{l_{\max}^3} \frac{l_{\max}^4}{4} = \frac{3}{4} l_{\max}. \tag{A.13}$$

In our case $l_{\max} = 44\,\mu\text{m}$, implying that $\langle l \rangle = 33\,\mu\text{m}$. This analysis does not, however, take into account that the larger l the smaller is the probability $\phi(l)$ that the BCBP will actually connect to the BC in question. This probability function $\phi(l)$ is much harder to estimate, but it explains why $\langle l \rangle \approx 20\,\mu\text{m}$ (see Section 3.4) instead of 33 µm.

References

[1] N. Kouyama and D. W. Marshak. The topographical relationship between two neuronal mosaics in the short wavelength-sensitive system of the primate retina. *Visual Neurosci*, 14:159–167, 1997.

[2] R. W. Rodieck. *The First Steps in Seeing*. Sinauer Associates, 1998.

[3] K. Franze, J. Grosche, S. N. Skatchkov, S. Schinkinger, C. Foja, D. Schild, O. Uckermann, K. Travis, A. Reichenback, and J. Guck. Müller cells are living optical fibers in the vertebrate retina. *P Natl Acad Sci USA*, 104:8287–8292, 2007.

[4] E. Sernagor, S. Eglen, B. Harris, and R. Wong, editors. *Retinal Development*. Cambridge University Press, 2006.

[5] H. Wässle and H. J. Riemann. The mosaic of nerve cells in the mammalian retina. *Proc R Soc Lond B*, 200:441–461, 1978.

[6] R. Marc and H. G. Sperling. Chromatic Organization of Primate Cones. *Science*, 196:454–456, 1977.

[7] N. Kouyama and D. W. Marshak. Bipolar Cells Specific for Blue Cones in the Macaque Retina. *J Neurosci*, 12:1233–1252, 1992.

[8] J. D. Mollon and J. K. Bowmaker. The spatial arrangement of cones in the primate fovea. *Nature*, 360:677–679, 1992.

[9] P. R. Martin and U. Grünert. Analysis of the Short Wavelength-Sensitive ("Blue") cone Mosaic in the Primate Retina: Comparison of New World and Old World Monkeys. *J Comp Neurol*, 406:1–14, 1999.

[10] L. Galli-Resta, E. Novelli, Z. Kryger, G. H. Jacobs, and B. E. Reese. Modelling the mosaic organization of rod and cone photoreceptors with a minimal-spacing rule. *Eur J Neurosci*, 11:1461–1469, 1999.

[11] X. Luo, K. K. Ghosh, P. R. Martin, and U. Grünert. Analysis of two types of cone bipolar cells in the retina of a New World monkey, the marmoset, *Callithrix jacchus*. *Visual Neurosci*, 16:707–719, 1999.

[12] K. Bumsted and A. Hendrickson. Distribution and Development of Short-Wavelength Cones Differ Between *Macaca* Monkey and Human Fovea. *J Comp Neurol*, 403:502–516, 1999.

[13] A. Roorda and D. R. Williams. The arrangement of the three cone classes in the living human eye. *Nature*, 397:520–522, 1999.

[14] M. Xiao and A. Hendrickson. Spatial and Temporal Expression of Short, Long/Medium, or Both Opsins in Human Fetal Cones. *J Comp Neurol*, 425:545–559, 2000.

[15] P. R. Martin, U. Grünert, and T. L. Chan. Spatial order in short-wavelength-sensitive cone photoreceptors: a comparative study of the primate retina. *J Opt Soc Am A*, 17:557–567, 2000.

[16] R. L. Rockhill, T. Euler, and R. H. Masland. Spatial order within but not between types of retinal neurons. *P Natl Acad Sci USA*, 97:2303–2307, 2000.

[17] A. Roorda, A. B. Metha, P. Lennie, and D. R. Williams. Packing arrangement of the three cone classes in primate retina. *Vision Res*, 41:1291–1306, 2001.

[18] A. F. Mack. Evidence for a columnar organization of cones, Müller cells, and neurons in the retina of a cichlid fish. *Neuroscience*, 144:1004–1014, 2007.

[19] K. C. Wikler and P. Rakic. Relation of an array of early-differentiating cones to the photoreceptor mosaic in the primate retina. *Nature*, 351:397–400, 1991.

[20] C. A. Curcion, K. A. Allen, K. R. Sloan, C. L. Lerea, J. B. Hurley, I. B. Klock, and A. H. Milam. Distribution and Morphology of Human Cone Photoreceptors Stained With Anti-Blue Opsin. *J Comp Neurol*, 312:610–624, 1991.

[21] K. Bumsted, C. Jasoni, Szél A., and A. Hendrickson. Spatial and Temporal Expression of Cone Opsins During Monkey Retinal Development. *J Comp Neurol*, 378:117–134, 1997.

[22] X. J. Zhan and J. B. Troy. Modeling cat retinal beta-cell arrays. *Visual Neurosci*, 17:23–39, 2000.

[23] S. J. Eglen, P. J. Diggle, and J. B. Troy. Homotypic constraints dominate positioning of on- and off-center beta retinal ganglion cells. *Visual Neurosci*, 22:859–871, 2005.

[24] S. J. Eglen and J. C. T. Wong. Spatial constraints underlying the retinal mosaics of two types of horizontal cells in cat and macaque. *Visual Neurosci*, 25:209–213, 2008.

[25] P. K. Ahnelt, E. Fernandez, O. Martinez, J. A. Bolea, and A. Kubber-Heiss. Irregular S-cone mosaics in felid retinas. Spatial interaction with axonless horizontal cells, revealed by cross correlation. *J Opt Soc Am A*, 17:580–588, 2000.

[26] S. J. Eglen, M. A. Raven, E. Tamrazian, and B. E. Reese. Dopaminergic Amacrine Cells in the Inner Nuclear Layer and Ganglion Cell Layer Comprise a Single Functional Retinal Mosaic. *J Comp Neurol*, 466:343–355, 2003.

[27] J. E. Cook and L. M. Chalupa. Retinal mosaics: new insights into an old concept. *Trends Neurosci*, 23:26–34, 2000.

[28] L. Galli-Resta, G. Resta, S.-S. Tan, and B. E. Reese. Mosaics of Islet-1-Expressing Amacrine Cells Assembled by Short-Range Cellular Interactions. *J Neurosci*, 17:7831–7838, 1997.

[29] B. E. Reese and L. Galli-Resta. The role of tangential dispersion in retinal mosaic formation. *Prog Retin Eye Res*, 21:153–168, 2002.

[30] S. J. Eglen, A. van Ooyen, and D. J. Willshaw. Lateral cell movement driven by dendritic interactions is sufficient to form retinal mosaics. *Network: Compu Neural Syst*, 11:103–118, 2000.

[31] C. Ruggiero, S. Benvenuti, S. Borchi, and M. Giacomini. Mathematical model of retinal mosaic formation. *Biosystems*, 76:113–120, 2004.

[32] C. Ruggiero, S. Benvenuti, and M. Giacomini. Mathematical Modeling of Retinal Mosaic Formation by Mechanical Interactions and Dendritic Overlap. *IEEE T Nanobiosci*, 6:180–185, 2007.

[33] A. P. Mariani. Bipolar cells in monkey retina selective for the cones likely to be blue-sensitive. *Nature*, 308:184–186, 1984.

[34] H. Kolb, K. A. Linberg, and S. K. Fisher. Neurons of the Human Retina: A Golgi Study. *J Comp Neurol*, 318:147–187, 1992.

[35] K. Klug, S. Herr, I. T. Ngo, P. Sterling, and S. Schein. Macaque Retina Contains an S-Cone OFF Midget Pathway. *J Neurosci*, 23:9881–9887, 2003.

[36] P. Ahnelt and H. Kolb. The Mammalian Photoreceptor Mosaic-adaptive Design. *Prog Retin Eye Res*, 19:711–777, 2000.

[37] S. Herr, K. Klug, and P. Sterling. Inner S-Cone Bipolar Cells Provide All of the Central Elements for S Cones in Macaque Retina. *J Comp Neurol*, 457:185–201, 2003.

[38] A. Szél, T. van Veen, and P. Röhlich. Retinal cone differentiation. *Nature*, 370:336, 1994.

[39] A. Szél, P. Röhlich, K. Mieziewska, G. Aguirre, and T. van Veen. Spatial and Temporal Differences Between the Expression of Short- and Middle-Wave Sensitive Cone Pigments in the Mouse Retina: A Developmental Study. *J Comp Neurol*, 331:564–577, 1993.

[40] P. J. Diggle. Displaced amacrine cells in the retina of a rabbit: analysis of a bivariate spatial point pattern. *J Neurosci Meth*, 18:115–125, 1986.

[41] R. W. Rodieck. The density recovery profile: A method for the analysis of points in the plane applicable to retinal studies. *Visual Neurosci*, 6:95–111, 1991.

[42] J. E. Cook. Spatial properties of retinal mosaics: An empirical evaluation of some existing measures. *Visual Neurosci*, 13:15–30, 1996.

[43] M. I. Chiu and J. Nathans. Blue Cones and Cone Bipolar Cells Share Transcriptional Specificity as Determined by Expression of Human Blue Visual Pigment-derived Transgenes. *J Neurosci*, 14:3426–3436, 1994.

[44] T. D. Lamb, S. P. Collin, and E. N. Jr. Pugh. Evolution of the vertebrate eye: opsins, photoreceptors, retina and eye cup. *Nat Rev Neurosci*, 8:960–975, 2007.

[45] B. E. Reese, B. D. Necessary, P. P. L. Tam, B. Faulkner-Jones, and S.-S. Tan. Clonal expansion and cell dispersion in the developing mouse retina. *Eur J Neurosci*, 11:2965–2978, 1999.